

FIGURE 2: The structure of the prehydrolysis state ( $M \cdot \text{ATP}$ ). The  $\gamma$ -phosphate of ATP is in a tetrahedral arrangement with its four oxygen atoms. A water molecule involved in hydrogen bonding with the  $\gamma$ -phosphate is denoted as  $w_1$ . We assume that this water is HOH1181 in the Fisher et al. structure (ref 5, 1MMD). The  $\beta$ - and  $\gamma$ -phosphate groups of ATP,  $\text{Mg}^{2+}$ , and the water molecule are shown in ball-and-stick form. Covalent bonds are shown as solid lines and hydrogen bonds and ionic interactions in dashed lines. Phosphorus, oxygen, hydrogen, and magnesium are depicted in yellow, red, blue, and green, respectively.

probably the electrical force between Arg-247 and the bound triphosphate moiety helps to close the cleft and to signal Trp-512. On the other hand, we felt that the close correlation between the presence of Glu at position 470 and hydrolysis probably meant that that particular residue had a role in catalysis. From the foregoing beginnings, we now commence to put together our hypothesis in the sequence that we suppose will be easiest to verify.

**The Prehydrolytic State.** Key features of relevant  $M \cdot \text{ATP}$  structure, i.e., of the situation at the active site, are in Figure 2 (abstracted from a Rayment snapshot of bound  $\text{MgADP} \cdot \text{BeF}_3^-$ ). Three oxygen atoms (1, 2, and 3) of the  $\gamma$ -phosphate group are bound and oriented by bound  $\text{Mg}^{2+}$ , the side chains of Asn-242 ( $N_{\delta 2}$ ) and Ser-245 ( $O_\gamma$ ) of Switch I, and Lys-183 of the P-loop, respectively. A single molecule of water,  $w_1$ , is attached to the guanidino group of Arg-247 ( $N_{\gamma 1}$ ), which interacts with a main chain carbonyl oxygen of Ser-246 of Switch I, and is attached to oxygen (3) of the  $\gamma$ -phosphate moiety of the bound nucleotide. (Note: The orientation of  $w_1$  is similar to that of a water molecule at the active site of transducin  $G_\alpha$  complexed with  $\text{GTP}\gamma\text{S}$  that mimics the ground state of bound  $\text{GTP}$  (11)). Because earlier we found a good correlation between the presence of Arg at position 247 and the rate of substrate binding to the active site (3), we speculated above that Arg-247 indirectly, perhaps by its electrical force, interacts with the  $\gamma$ -phosphate moiety via  $w_1$ , and so for this reason this positive residue is important for binding substrate to the active site. In this ground state, however,  $w_1$  does not yet have the position to act (see below).

**Closure of the Nucleotide-Binding Cleft.** Figure 3 depicts diagrammatically how we think this cleft closes: (A) repeats the same stage depicted in Figure 2; (B) is an intermediate stage; and (C) is the final stage. Comparison of the three stages implies that on closure there is a big structural change in Switch II (in light blue), but none in Switch I (in black).

In Figure 3A the cleft is still open, so the Switch II residues, excepting Asp-465, do not interact with either the bound nucleotide or the bound  $\text{Mg}^{2+}$  at this stage.  $\text{Mg}^{2+}$  is very important in closure because of its location in the cleft. It is central in chelating the  $\beta$ - and  $\gamma$ -phosphates of the

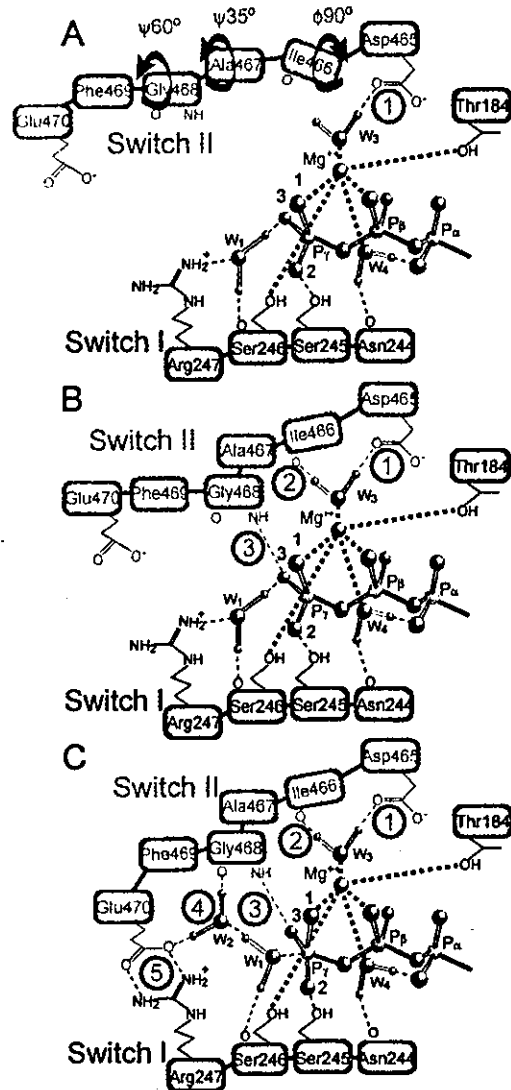


FIGURE 3: The closing process of the nucleotide-binding cleft. A series of diagrams show the disposition in space of the Switch II strand (colored light blue) at three different times after nucleotide binds to the active site: A, the early stage; B, the intermediate stage; and C, the final stage. In the diagrams, we also show how the  $\gamma$ -phosphate moieties of bound nucleotide are associated with the strand. We assume that  $w_1$  in A is HOH1181 in the Fisher et al. structure (ref 5, 1MMD) and that  $w_1$  and  $w_2$  in C take the place of the terminal oxygen atom of the vanadate moiety and that of HOH697, respectively, in the Smith and Rayment structure (ref 6, 1VOM). Three curved arrows show the general direction in which relevant Ramachandran angles change in the transition from the A to the B state (the angle and the amount of its change are given). The progressive attachments of the Switch II strand occur in the sequence given by the circled numeral. Covalent bonds are shown as solid lines and hydrogen bonds and ionic interactions in dashed lines. Coordinated interactions with the  $\text{Mg}^{2+}$  of bound nucleotide are shown as green, thick dashed lines. Phosphorus, oxygen, hydrogen, and magnesium are depicted in yellow, red, blue, and green, respectively.

nucleotide, and in its coordination sphere are six ligands in octahedral geometry. Also,  $\text{Mg}^{2+}$  is connected with both the P-loop via  $O_{\gamma 1}$  of Thr-184 and Switch I via  $O_\gamma$  of Ser-246. Two water molecules are coordinated to  $\text{Mg}^{2+}$ . One,  $w_4$ , interacts with the main chain carbonyl oxygen of Asn-244, and also bonds to an oxygen atom of the  $\alpha$ -phosphate group. One of the hydrogen atoms of another water molecule,  $w_3$ , interacts with the side chain of Asp-465 ( $O_{\delta 2}$ ). This fact,

and his own work on mutations, led Sutoh to suggest that Asp-465 is important in nucleotide binding (24). We propose that  $w_1$  retains its attachment to Switch I, and that, by virtue of the intervention of  $w_3$  (which inserts between the  $Mg^{2+}$  associated with Switch I via the bound nucleotide and a carboxyl oxygen atom of Asp-465 of Switch II), the closing of the cleft is initiated. The three curved arrows in Figure 3A indicate the direction in which the relative Ramachandran angles change in the transition between states. When Ile-466 rotates (permitted by the flexibility of the Switch II loop) in such a way that its Ramachandran angle  $\phi$  increases by  $90^\circ$ , the oxygen atom of its main chain carbonyl group moves toward  $w_3$ , and can now form a bond with the other hydrogen atom of the  $w_3$ . Accompanying changes in the  $\phi$  angles of Ala-467 and Gly-468 (see Figure 3A) create an interaction between the main chain amide hydrogen of Gly-468 and the  $\gamma$ -phosphate moiety of the bound nucleotide. (See Figure 3B.) At this stage,  $w_2$  first appears in the crystallographic image of the phosphate pocket of the enzyme. It is hydrogen-bonded to the main chain carbonyl oxygen of Gly-468, and to one of the two oxygen atoms of the carboxyl group of Glu-470 ( $O_{e1}$ ). See Figure 3C. As earlier noted, Trp-512 is remotely connected to Switch II in the active site; it is at this stage that Trp-512 is "informed" and increases its fluorescence. (See Scheme 1.)

Although, strictly speaking, observations of the sort we are citing cannot be put in cause-to-effect relations, cleft closure is closely correlated in time with at least two other important events. One is that, with closure, force appears to be transmitted via the long  $\alpha$ -helix, across the so-called "converter" region, to what appears to be the myosin "lever arm" (7). It is known that in a myosin "motor", the mechanical working (power) stroke is time-correlated with the phosphate release step that follows hydrolysis (Figure 4). Also, Sutoh et al. (25) showed that a large angle change of the lever arm occurring during  $M \cdot ATP \rightarrow M^* \cdot ATP$  is necessary for the reverse of the power stroke motion. Other events also associated with closure (to be discussed later) are a hydrogen-bond interaction between Gly-468 and an oxygen atom of the  $\gamma$ -phosphate, and the formation of the salt-bridge between side chains of Arg-247 and Glu-470—all crucial for setting up catalysis.

**The Transition State for Hydrolysis.** In the snapshot taken to represent the situation at the time of hydrolysis ( $MgADP \cdot VO_4^-$  bound to the active site), the cleft is closed and there are two molecules of water bound in the  $\gamma$ -phosphate pocket (6). We suppose (Figure 3C) that movement of Glu-470 permits its bridging toward the guanidino group of Arg-247, which then releases its water,  $w_1$ , destined to become the "lytic" water. One of the hydrogen atoms of this water, initially bonded to an oxygen atom of the  $\gamma$ -phosphate group, then interacts with the oxygen atom of a new, intruding water,  $w_2$ . The other hydrogen atom remains bonded to the main chain carbonyl oxygen of Ser-246. A result of making this critical conjecture is that then  $w_1$  ends up partially positioned and oriented to carry out its attack on the  $\gamma$ -phosphorus (cf., the analogous location of the lytic water in the active site of transition-state transducin  $G_\alpha$  (11)). Even at this stage, however, our conjecture already responds to certain requirements. It provides explanations of why two water molecules are seen in the snapshot of the transition state (6), why the ability of a system to catalyze hydrolysis

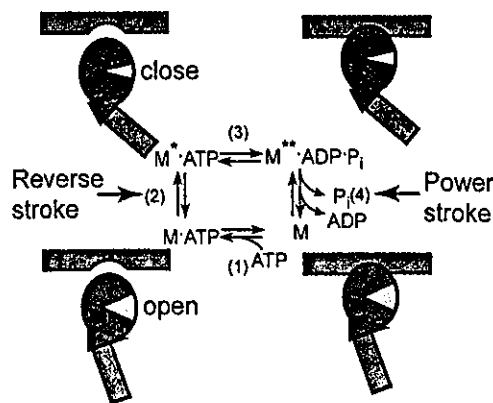


FIGURE 4: Some important transformations during the ATPase cycle. Chemically, myosin (M) binds to ATP, hydrolyzes it to ADP +  $P_i$ , and releases the products. To function in muscle contraction myosin must undergo (a) a conformational change that switches between actin-binding and actin-release states, and (b) a conformational change that swings the lever arm for contraction ("power stroke"). Presumably, a sequence that must occur in muscle is (1) the conformational change that allows release from actin, (2) the conformational change that reverse swings the lever arm, (3) the conformational change to the actin-binding state, and (4) the conformational change that swings the lever arm in the power stroke. In this article, however, we are only concerned with conformational change (2) and the following hydrolysis. As the product release from  $M^{**} \cdot ADP \cdot P_i$ , at which the power stroke occurs, is greatly accelerated by actin, it seems reasonable to assume that the transition to the actin-binding state occurs in the state  $M^{**} \cdot ADP \cdot P_i$ . However, the conformational change during this transition is not well clarified yet. The reverse and power strokes occur at the stages indicated. This figure also denotes the relationship of myosin to actin (free or bound). The motor domain is depicted in red, the converter in green, the lever arm in blue, the nucleotide-binding cleft in yellow, and the actin filament in violet. A long, conserved  $\alpha$ -helix that connects between the binding cleft and the converter is shown as a spiral in the motor domain.

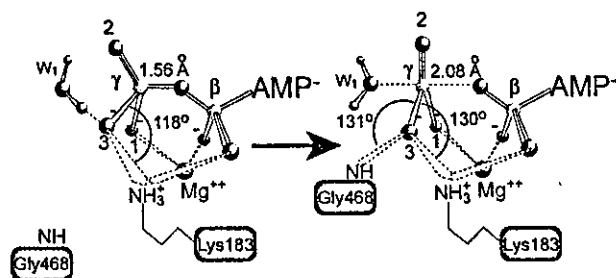


FIGURE 5: A mechanism for the change of the  $\gamma$ -phosphate configuration. The left and right diagrams represent the tetrahedral and the trigonal bipyramidal structures, respectively. The  $\beta$ - and  $\gamma$ -phosphate of ATP, the  $Mg^{2+}$ , and a water molecule are shown as a ball-and-stick model. Oxygen atoms interacted with  $Mg^{2+}$ , Ser-245, and Lys-183 are denoted as 1, 2, and 3, respectively. Angles of  $P_\gamma-O-N_\zeta$  of Lys-183 and  $P_\gamma-O-N_{main\ chain}$  of Gly-468, and the distance between the  $\gamma$ -phosphorus and the  $\beta$ - $\gamma$  bridging oxygen are given from the crystal structures (1MMD for the left diagram and 1VOM for the right diagram).

is tightly correlated to the presence of Glu at position 470 (3), and why the Rayment (6) surmise of a functional role for a "water network" was prophetic.

Although already partly positioned by  $w_2$  and Ser-246, we believe that  $w_1$  is not yet at its final attack position and that its final positioning results from the shift of the  $\gamma$ -phosphate structure from its tetrahedral to its trigonal bipyramidal configuration. As already stated, we cannot assign cause-to-effect relationships, but do think that the final positioning

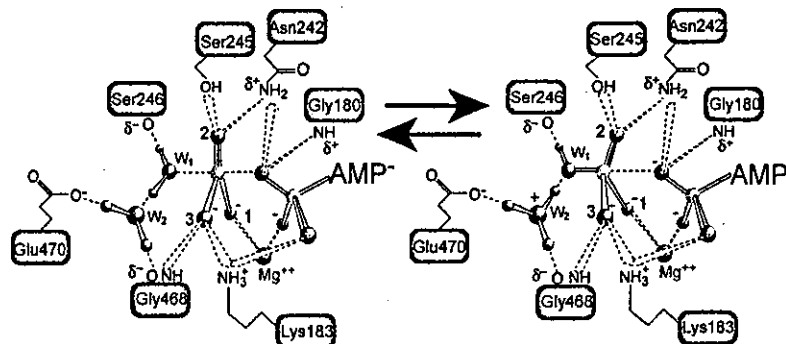


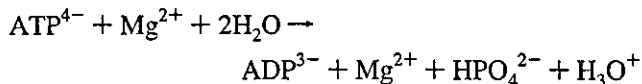
FIGURE 6: The transfer of a proton from  $w_1$  to  $w_2$  and the production of  $P_i$  and  $H_3O^+$ . The left and right diagrams represent the structures for the transition and posthydrolysis states, respectively.  $\delta^+$  and  $\delta^-$  indicate positive and negative charges, respectively, which are induced by the resonance structures of the peptide bond. Covalent bonds are shown as filled lines, and hydrogen bonds and ionic interactions in dashed lines. The  $\beta$ - and  $\gamma$ -phosphates of ATP,  $Mg^{2+}$ , and two water molecules are shown as a ball-and-stick model.

ends a series of identifiable events. It will be recalled that Gly-468 is the only residue whose interaction with the  $\gamma$ -phosphate is induced by the cleft closure. One of possible speculations about the conformational change of the  $\gamma$ -phosphate now follows. As is well-known, the normal angle of separation between two oxygen bonds is about  $105^\circ$ . In the prehydrolysis state ( $MgADP \cdot BeF_x$  bound to the active site), this angle in  $P_\gamma-O-N_\zeta$  of Lys-183 is  $118^\circ$  (quasi normal) (left, Figure 5). So, we suggest that when the cleft is open (Gly-468 is away from the  $\gamma$ -phosphate), the tetrahedral is preferred over the trigonal bipyramidal configuration. In the transition state for hydrolysis ( $MgADP \cdot VO_4^-$  bound to the active site), the  $P_\gamma-O-N_\zeta$  angle becomes significantly larger, viz.,  $130^\circ$  (right, Figure 5). In contrast, the  $P_\beta-O-N_\zeta$  angle of the same Lys-183 remains essentially constant during the same transit ( $111^\circ$  vs  $114^\circ$ ). As cited earlier (Figure 3B), the main chain amide nitrogen ( $N_{main\ chain}$ ) of Gly-468 creates an interaction with oxygen (3) of the  $\gamma$ -phosphate during the transit to the transition state. The  $P_\gamma-O-N_{main\ chain}$  angle of Gly-468 was  $131^\circ$ , essentially the same as the new  $P_\gamma-O-N_\zeta$  angle of Lys-183. This circumstance suggests a reason why interaction of Gly-468 with the  $\gamma$ -phosphate energetically disposes  $\gamma$ -phosphate to leave from the bridging oxygen between  $\beta$ - and  $\gamma$ -phosphates, and at the same time changes its configuration. If this speculation is granted, several observations are conveniently explained, e.g., why the trigonal bipyramidal configuration is observed only in structures in which the cleft is closed (5, 6), why the K183A<sup>5</sup> system can catalyze hydrolysis even though Lys-183 is involved in the catalysis (unpublished observations), and why, as earlier observed (1), the G468A system exhibits neither steady-state ATPase nor an initial phosphate burst.

**"Two-Water" Hypothesis of How Myosin Catalyzes ATPase.** As described in the foregoing section,  $w_1$  is now oriented to carry out its attack on the  $\gamma$ -phosphate, and, on the other side, the  $\gamma$ -phosphate is readied for the attack from  $w_1$  by changing its configuration into a trigonal bipyramidal. Now, we deal with the question of how hydrolysis proceeds to produce  $P_i$  and ADP. No crystal structure of the posthydrolysis state is available, but we can make some guesses about the passage from the transition state to the post-

hydrolysis state. Our proposal resembles catalysis by the GTPase system. Coleman and Sprang (9) have reviewed the latter system, explaining the participation of highly conserved Gln and Arg (in  $G_{1\alpha}$ , Gln-204 and Arg-178). In our hypothesis, Glu-470- $w_2$ -Gly-468 and Asn-242, respectively, play analogous roles. The essential transformations are depicted in Figure 6. On the left is the transition state, and on the right is a state resulting from hydrolysis. When the  $\gamma$ -phosphate approaches,  $w_1$  splits, the resulting hydroxyl moiety attacks the  $\gamma$ -phosphate (to form  $P_i$ ), and the resulting proton transfers to  $w_2$  (to form  $H_3O^+$ ). The positive charge developed at  $w_2$  is stabilized by both the carboxyl group of Glu-470 and the main chain carbonyl oxygen of Gly-468, both of which are negatively charged (denoted as  $\delta^-$ ). After  $P_i$  leaves, the terminal oxygen atom of the  $\beta$ -phosphate group of ADP is also ionized. This negative charge is neutralized by the side chain of Asn-242 ( $N_{\delta 2}$ ) and the main chain amide of Gly-180, both of which are positively charged (denoted as  $\delta^+$ ). This model is consistent with crystallographic observations suggesting that Asn-242 and Gly-180 both interact with the bridging oxygen atom of the  $\beta$ -phosphate (5, 6), and also harmonizes with our results that in the N242A system both steps of  $M^{**} \cdot ADP \cdot P_i \rightarrow M^* \cdot ADP + P_i$  and the displacement of  $M^* \cdot ADP$  are 10 times faster than in the wild-type system (unpublished observations). Our proposal thus resolves the long-standing conundrum about how catalysis seems to be carried out absent an obvious hydrogen acceptor.

Earlier kinetic studies have shown that per mole of ATP hydrolyzed at pH 8.0, one mole of protons is produced, at the rate limitation corresponding to  $P_i$  release (12, 13, 26). Because protons in water exist as hydronium ions, the appropriate chemical equation is



It seems important that our hypothesis accounts stoichiometrically for each of the chemical species in this equation. These kinetic studies have also shown that for the enzyme-bound system, the equilibrium constant for hydrolysis is near to unity (12, 13, 26), so it is plausible to assume that at this stage there is a rapid interconversion between similarly weighted structures and thus to account for how experiments in  $H_2^{18}O$  yield  $^{18}O$ -labeling of more than one per mole (27-29). This feature of the catalysis may or may not bear on

<sup>5</sup> A mutant is represented by a one-letter expression of the original amino acid residue prior to its sequence number, and that of the mutated residue following to its number, i.e., R183A, G468A, and N242A.

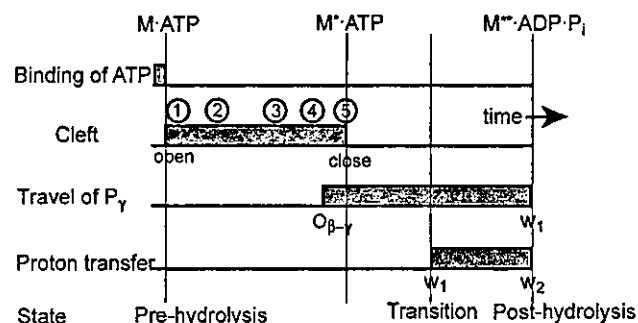


FIGURE 7: A chronological sequence of events during ATP hydrolysis. The period of each event is shown as a gray zone. 1, 2, 3, 4, and 5 represent coordination of Asp-465 to  $Mg^{2+}$  via  $w_3$ , Ramachandran angle changes at Ile-466, Ala-467, and Gly-468, hydrogen-bonding of Gly-468 to an oxygen of the  $\gamma$ -phosphate, trapping of  $w_2$  between Gly-468 and Glu-470, and salt-bridge formation between Glu-470 and Arg-247, respectively.

how excess labeling of  $P_i$  is interpreted. It is conceivable that although the crystallographically observed number of water molecules inside of the cleft is small, the actual number of water molecules in free exchange with the cleft may be large. In that case, the usual mechanism (interconversion and random labeling) can be invoked.

The name that we use for our proposal stems from our thinking that, in essence, two contiguous water molecules are involved in catalysis, i.e., one becomes the lytic water and the other is the proton acceptor. However, as we have attempted to show, this simplification is embedded in a program of complicated, well-coordinated processes that together constitute "myosin catalysis". Some tracks in time are shown in Figure 7. If we commence a myosin cycle with the binding of ATP to an empty active site (forming of  $M \cdot ATP$ ), we must think of the cleft closing, which is followed by two processes. One is hydrogen-bonding of the main chain nitrogen atom of Gly-468 to an oxygen atom of the  $\gamma$ -phosphate (denoted as 3 in Figure 7), which affects the choice of the  $\gamma$ -phosphate configuration. As a result, the  $\gamma$ -phosphorus begins its long travel from the  $\beta$ - $\gamma$  bridging oxygen to  $w_1$ ; in other words, inversion of the  $\gamma$ -phosphate begins. Other processes following cleft closing are Arg-247 and Glu-470 forming of the salt-bridge (denoted as 5 in Figure 7), trapping of  $w_2$  by its hydrogen-bonding with both Glu-470 and Gly-468,  $w_1$  leaving from the guanidino group of Arg-247, and hydrogen-bonding between  $w_1$  and  $w_2$ . Finally, a nucleophilic attack of  $w_1$  on the  $\gamma$ -phosphate, coupled with the proton transfer from  $w_1$  to  $w_2$ , occurs to produce  $P_i$  and  $H_3O^+$ .

While plausible variants of the "two-water" idea are conceivable, as are elaborations of the role of Lys-183 (30, 31), such a variant must contend with the experimental fact that the mutated system with alanine in place of lysine still accomplishes hydrolysis. Also, any variant must explain why it is necessary to have glutamic acid at 470 to accomplish hydrolysis.

#### ACKNOWLEDGMENT

We are grateful to Professor H. M. Martinez for his helpful counsel and Professors I. Rayment and D. McKay for significant improvements in our manuscript.

#### REFERENCES

- Onishi, H., Morales, M. F., Kojima, S., Katoh, K., and Fujiwara, K. (1997) Functional transitions in myosin: role of highly conserved Gly and Glu residues in the active site. *Biochemistry* 36, 3767–3772.
- Onishi, H., Kojima, S., Katoh, K., Fujiwara, K., Martinez, H. M., and Morales, M. F. (1998) Functional transitions in myosin: formation of a critical salt-bridge and transmission of effect to the sensitive tryptophan. *Proc. Natl. Acad. Sci. U.S.A.* 95, 6653–6658.
- Onishi, H., Ohki, T., Mochizuki, N., and Morales, M. F. (2002) Early stages of energy transduction by myosin: roles of Arg in switch I, of Glu in switch II, and of the salt-bridge between them. *Proc. Natl. Acad. Sci. U.S.A.* 99, 15339–15344.
- Rayment, I., Rypniewski, W. R., Schmidt-Bäse, K., Smith, R., Tomchick, D. R., Benning, M. M., Winkelmann, D. A., Wesenberg, G., and Holden, H. M. (1993) Three-dimensional structure of myosin subfragment-1: a molecular motor. *Science* 261, 50–58.
- Fisher, A. J., Smith, C. A., Thoden, J. B., Smith, R., Sutoh, K., Holden, H. M., and Rayment, I. (1995) X-ray structures of the myosin motor domain of *Dictyostelium discoideum* complexed with  $MgADP \cdot BeFx$  and  $MgADP \cdot AlF_4^-$ . *Biochemistry* 34, 8960–8972.
- Smith, C. A., and Rayment, I. (1996) X-ray structure of the magnesium(II)·ADP·vanadate complex of the *Dictyostelium discoideum* myosin motor domain to 1.9 Å resolution. *Biochemistry* 35, 5404–5417.
- Dominguez, R., Freyzon, Y., Trybus, K. M., and Cohen, C. (1998) Crystal structure of a vertebrate smooth muscle myosin motor domain and its complex with the essential light chain: visualization of the pre-power stroke state. *Cell* 94, 559–571.
- Houdusse, A., Kalabokis, V. N., Himmel, D., Szent-Györgyi, A. G., and Cohen, C. (1999) Atomic structure of scallop myosin subfragment S1 complexed with  $MgADP$ : a novel conformation of the myosin head. *Cell* 97, 459–470.
- Coleman, D. E., and Sprang, S. R. (1999) Reaction dynamics of G-protein catalyzed hydrolysis of GTP as viewed by X-ray crystallographic snapshots of  $G_{\alpha 1}$ . *Methods Enzymol.* 308, 70–92.
- Coleman, D. E., Berghuis, A. M., Lee, E., Linder, M. E., Gilman, A. G., and Sprang, S. R. (1994) Structures of active conformations of  $G_{\alpha 1}$  and the mechanism of GTP hydrolysis. *Science* 265, 1405–1412.
- Sondek, J., Lambright, D. G., Noel, J. P., Hamm, H. E., and Sigler, P. B. (1994) GTPase mechanism of Gproteins from the 1.7-Å crystal structure of transducin  $\alpha$ -GDP·AlF<sub>4</sub><sup>-</sup>. *Nature* 372, 276–279.
- Bagshaw, C. R., and Trentham, D. R. (1974) The characterization of myosin-product complexes and of product-release steps during the magnesium ion-dependent adenosine triphosphatase reaction. *Biochem. J.* 141, 331–349.
- Bagshaw, C. R., Eccleston, J. F., Eckstein, F., Goody, R. S., Gutfreund, H., and Trentham, D. R. (1974) The magnesium ion-dependent adenosine triphosphatase of myosin. Two-step processes of adenosine triphosphate association and adenosine diphosphate dissociation. *Biochem. J.* 141, 351–364.
- Morita, F. (1967) Interaction of heavy meromyosin with substrate. I. Difference in ultraviolet absorption spectrum between heavy meromyosin and its Michaelis–Menten complex. *J. Biol. Chem.* 242, 4501–4506.
- Werber, M. M., Szent-Györgyi, A. G., and Fasman, G. D. (1972) Fluorescence studies on heavy meromyosin-substrate interaction. *Biochemistry* 11, 2872–2883.
- Johnson, W. C., Jr., Bivin, D. B., Ue, K., and Morales, M. F. (1991) A search for protein structural changes accompanying the contractile interaction. *Proc. Natl. Acad. Sci. U.S.A.* 88, 9748–9750.
- Hiratsuka, T. (1992) Spatial proximity of ATP-sensitive tryptophanyl residue(s) and Cys-697 in myosin ATPase. *J. Biol. Chem.* 267, 14949–14954.
- Batra, R., and Manstein, D. J. (1999) Functional characterisation of *Dictyostelium* myosin II with conserved tryptophanyl residue 501 mutated to tyrosine. *Biol. Chem.* 380, 1017–1023.
- Yengo, C. M., Chrin, L. R., Rovner, A. S., and Berger, C. L. (2000) Tryptophan 512 is sensitive to conformational changes in the rigid relay loop of smooth muscle myosin during the  $MgATPase$  cycle. *J. Biol. Chem.* 275, 25481–25487.

20. Park, S., and Burghardt, T. P. (2002) Tyrosine mediated tryptophan ATP sensitivity in skeletal myosin. *Biochemistry* 41, 1436–1444.
21. Onishi, H., Konishi, K., Fujiwara, K., Hayakawa, K., Tanokura, M., Martinez, H. M., and Morales, M. F. (2000) On the tryptophan residue of smooth muscle myosin that responds to binding of nucleotide. *Proc. Natl. Acad. Sci. U.S.A.* 97, 11203–11208.
22. Malnasi-Csizmadia, A., Woolley, R. J., and Bagshaw, C. R. (2000) Resolution of conformational states of *Dictyostelium* myosin II motor domain using tryptophan (W501) mutants: implications for the open-closed transition identified by crystallography. *Biochemistry* 39, 16135–16146.
23. Gulick, A. M., Bauer, C. B., Thoden, J. B., and Rayment, I. (1997) X-ray structures of the MgADP, MgATP $\gamma$ S, and MgAMPPNP complexes of the *Dictyostelium discoideum* myosin motor domain. *Biochemistry* 36, 11619–11628.
24. Sasaki, N., Shimada, T., and Sutoh, K. (1998) Mutational analysis of the switch II loop of *Dictyostelium* myosin II. *J. Biol. Chem.* 273, 20334–20340.
25. Suzuki, Y., Yasunaga, T., Ohkura, R., Wakabayashi, T., and Sutoh, K. (1998) Swing of the lever arm of a myosin motor at the isomerization and phosphate-release steps. *Nature* 396, 380–383.
26. Lymn, R. W., and Taylor, E. W. (1971) Mechanism of adenosine triphosphate hydrolysis by actomyosin. *Biochemistry* 10, 4617–4624.
27. Levy, H. M., and Koshland, D. E. (1959) Mechanism of hydrolysis of adenosinetriphosphate by muscle proteins and its relation to muscular contraction. *J. Biol. Chem.* 234, 1102–1107.
28. Webb, M. R., and Trentham, D. R. (1981) The mechanism of ATP hydrolysis catalyzed by myosin and actomyosin, using rapid reaction techniques to study oxygen exchange. *J. Biol. Chem.* 256, 10910–10916.
29. Bowater, R., Zimmerman, R. W., and Webb, M. R. (1990) Kinetics of ATP and inorganic phosphate release during hydrolysis of ATP by rabbit skeletal actomyosin subfragment 1, Oxygen exchange between water and ATP or phosphate. *J. Biol. Chem.* 265, 171–176.
30. Kagawa, H., and Mori, K. (1999) Molecular orbital study of the interaction between MgATP and the myosin motor domain: The highest occupied molecular orbitals indicate the reaction site of ATP hydrolysis. *J. Phys. Chem. B* 103, 7346–7352.
31. Minehardt, T. J., Marzari, N., Cooke, R., Pate, E., Kollman, P. A., and Car, R. (2002) A classical and ab initio study of the interaction of the myosin triphosphate binding domain with ATP. *Biophys. J.* 82, 660–675.

BI040002M

# A Novel Actin Bundling/Filopodium-forming Domain Conserved in Insulin Receptor Tyrosine Kinase Substrate p53 and Missing in Metastasis Protein\*<sup>§</sup>

Received for publication, August 25, 2003, and in revised form, December 26, 2003  
Published, JBC Papers in Press, January 29, 2004, DOI 10.1074/jbc.M309408200

Akiko Yamagishi, Michitaka Masuda†, Takashi Ohki, Hirofumi Onishi, and Naoki Mochizuki

From the Department of Structural Analysis, National Cardiovascular Center Research Institute, 5-7-1 Fujishiro-dai, Suita, Osaka 565-8565, Japan

Insulin receptor tyrosine kinase substrate p53 (IRSp53) has been identified as an SH3 domain-containing adaptor that links Rac1 with a Wiskott-Aldrich syndrome family verprolin-homologous protein 2 (WAVE2) to induce lamellipodia or Cdc42 with Mena to induce filopodia. The recruitment of these SH3-binding partners by IRSp53 is thought to be crucial for F-actin rearrangements. Here, we show that the N-terminal predicted helical stretch of 250 amino acids of IRSp53 is an evolutionarily conserved F-actin bundling domain involved in filopodium formation. Five proteins including IRSp53 and missing in metastasis (MIM) protein share this unique domain and are highly conserved in vertebrates. We named the conserved domain IRSp53/MIM homology domain (IMD). The IMD has domain relatives in invertebrates but does not show obvious homology to any known actin interacting proteins. The IMD alone, derived from either IRSp53 or MIM, induced filopodia in HeLa cells and the formation of tightly packed parallel F-actin bundles *in vitro*. These results suggest that IRSp53 and MIM belong to a novel actin bundling protein family. Furthermore, we found that filopodium-inducing IMD activity in the full-length IRSp53 was regulated by active Cdc42 and Rac1. The SH3 domain was not necessary for IMD-induced filopodium formation. Our results indicate that IRSp53, when activated by small GTPases, participates in F-actin reorganization not only in an SH3-dependent manner but also in a manner dependent on the activity of the IMD.

the central nervous system (1–3). The protein contains a unique N-terminal 250-amino acid stretch, a half-Cdc42/Rac interactive binding (CRIB) motif, a proline-rich domain, a Src homology 3 (SH3) domain, and a WW domain-binding motif (WWB). IRSp53 is directly regulated by Rho family small GTPases Rac1 and Cdc42 and provides a molecular link between these GTPases and the actin cytoskeleton regulators Wiskott-Aldrich syndrome protein (WASP) family verprolin homologous protein 2 (WAVE2) and mammalian enabled (Mena), which are involved in the formation of lamellipodia (4, 5) and filopodia (6, 7). Active Cdc42 binds to the half-CRIB motif (6, 7), whereas Rac1 binds to the unique N-terminal domain (8). The association of Rac1 or Cdc42 is proposed to liberate the C-terminal SH3 domain masked intramolecularly by its N terminus, thereby allowing the SH3 domain to interact with its binding partners (4, 7, 9). Thus, the SH3 domain is thought to be essential for IRSp53-mediated actin reorganization. However, the N-terminal half of IRSp53 lacking the SH3 domain was reported to induce neurite outgrowth in a neuroblastoma cell line (6) and filopodia in B16 melanoma cells (10), suggesting that IRSp53 promotes actin reorganization independently of SH3 domain-mediated intermolecular interactions.

Recently, a novel monomeric actin-binding protein, missing in metastasis protein (MIM), containing a WASP homology 2 (WH2) domain in the C terminus, was reported in human and mouse (11–13) and found to share the unique N-terminal domain with IRSp53 (13). We found that the N-terminal domains of MIM and IRSp53 also share other characteristic features; the predicted secondary structures are almost purely helical (see Ref. 9 for IRSp53), and the estimated isoelectric points are around 9. MIM induces actin cytoskeleton reorganization in cultured cells. This activity is not dependent on the C-terminal half (13), suggesting that the N-terminal half containing the IRSp53 homologous domain plays a key role in actin reorganization.

Here we show that IRSp53 and MIM belong to an evolutionarily related protein family sharing a well conserved N-terminal helical domain (IRSp53/MIM homology domain (IMD)) as a key constituent. We investigated the role of the IMD in actin reorganization. Our results indicate that the IMDs of IRSp53 and MIM induce filopodia in cultured cells and form tightly packed F-actin bundles *in vitro*. The filopodium forming activity of the IMD in full-length IRSp53 is regulated by small GTPases. Thus, upon association with active Rac1 or Cdc42, IRSp53 can induce actin cytoskeleton reorganization by dual mechanisms: the SH3-mediated recruitment of F-actin regulators and the action of the novel actin bundling domain in the N terminus. Both mechanisms may work synergistically or additively in controlling cortical actin dynamics.

Insulin receptor tyrosine kinase substrate p53 (IRSp53),<sup>1</sup> also known as brain-specific angiogenesis inhibitor 1-associated protein 2, is a multifunctional adaptor protein enriched in

\* This work was supported in part by grants from the Ministry of Health, Labour and Welfare, from the Organization for Pharmaceutical Safety and Research of Japan, Special Coordination Funds for Promoting Science and Technology from the Ministry of Education, Culture, Sports, Science and Technology, and from the Human Science Foundation of Japan. The costs of publication of this article were defrayed in part by the payment of page charges. This article must therefore be hereby marked "advertisement" in accordance with 18 U.S.C. Section 1734 solely to indicate this fact.

<sup>§</sup> The on-line version of this article (available at <http://www.jbc.org>) contains supplemental data.

† To whom correspondence should be addressed. Fax: 81-6-6835-5461; E-mail: [masuda61@ri.ncvc.go.jp](mailto:masuda61@ri.ncvc.go.jp).

<sup>1</sup> The abbreviations used are: IRSp53, insulin receptor tyrosine kinase substrate p53; CRIB, Cdc42/Rac interactive binding; MIM, missing in metastasis protein; SH3, Src homology 3; WWB, WW domain-binding motif; WASP, Wiskott-Aldrich syndrome protein; WH2, WASP homology 2; IMD, IRSp53/MIM homology domain; GFP, green fluorescent protein; GST, glutathione S-transferase; IRTKS, insulin receptor tyrosine kinase substrate; aa, amino acids.

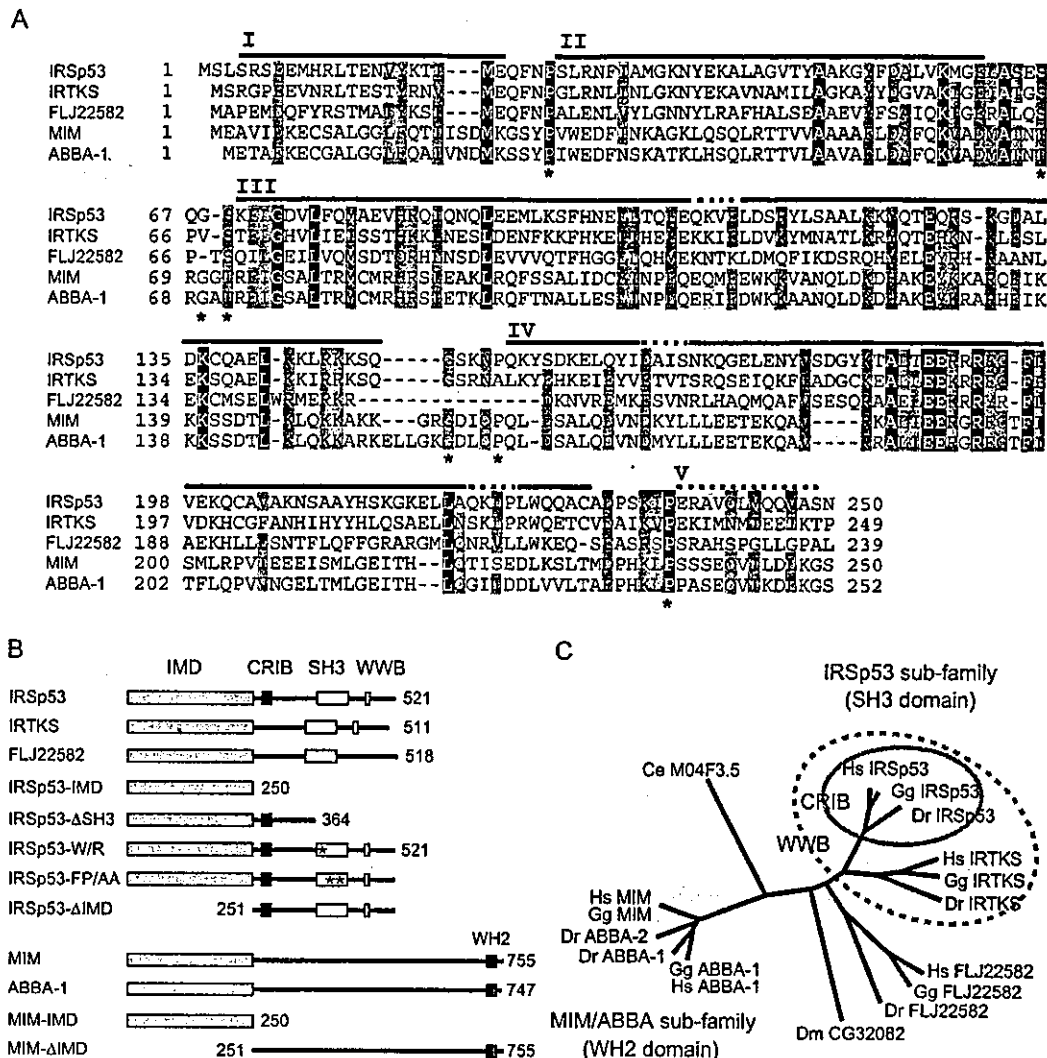


**FIG. 1. The N-terminal helical domains of IRSp53 and MIM are evolutionarily conserved.** *A*, amino acid sequence alignment of the N terminus of known human proteins containing the IMD. The areas where all of the residues are identical are shown in **black**; highly conserved residues are **dark gray**; weakly conserved residues are **light gray**. The numbered lines on the sequence show the predicted helical stretches of IRSp53. The asterisks show conserved helix-breaking residues. *B*, schematic representation of the domain composition of human proteins containing the IMD. IRSp53 contains a half-CRIB motif (CRIB), an SH3 domain (SH3), and a WWB. IRTKS lacks CRIB, whereas FLJ22582 lacks both CRIB and WWB. MIM and ABBA-1 each contains a WH2 domain in the C terminus. Truncated fragments of IRSp53 and MIM used in this study are also shown. The positions of mutation in the SH3 domain are indicated by asterisks. *C*, unrooted tree of IMDs based on ClustalW alignment. Species used: human (*Hs*), chicken (*Gg*), zebra fish (*Dr*), *D. melanogaster* (*Dm*), and *C. elegans* (*Ce*). Members containing a WWB and a half-CRIB motif are encircled by dotted circles and continuous circles, respectively. See supplemental Fig. 6 for a full version of the alignment, which was further modified to improve the alignment in the N termini and to match with the predicted helical structures.

#### EXPERIMENTAL PROCEDURES

**Data Base Search**—Proteins homologous to IRSp53 and MIM were identified in the GenBank™ data base using BLAST on the National Center for Biotechnology Information web site and on the GenomeNet web site. The details of sequences thus retrieved are described in the supplemental data. The Clustalw engine at the GenomeNet Web site was used to align amino acid sequences and to construct phylogenetic trees. The secondary structures of proteins were predicted by 3D-PSSM (14).

**Plasmids**—The IRSp53 expression vector pEF-BOS-Myc-IRSp53 (human isoform 1) was kindly donated by Dr. Miki (4). cDNAs encoding full-length IRSp53 (amino acids (aa) 1–521), IRSp53-ASH3 (aa 1–364), IRSp53-IMD (aa 1–250), and IRSp53-ΔIMD (aa 251–521) (see Fig. 1*B*) were amplified by PCR and inserted into pEGFP-C1 (Clontech), pCXN2-FLAG (15), and pGEX-4T3 or 6P3 (Amersham Biosciences) vectors. The DNA fragments encoding IRSp53 where Arg was substituted for Trp<sup>413</sup> or Ala for both Phe<sup>427</sup> and Pro<sup>428</sup> in the SH3 domain, hereafter referred to as IRSp53-W/R or IRSp53-FP/AA, were amplified by PCR and ligated into pEGFP-C1. cDNA of Rac1V12, Rac1N17, Cdc42V12, or Cdc42N17 was subcloned into pIRM21, an expression vector expressing FLAG-tagged protein and internal ribosomal entry site-driven dsFP593 (16). A cDNA clone encoding the N-terminal frag-

ment (aa 1–430) of human MIM was obtained by PCR from a human brain cDNA library (Clontech). The cDNA encoding C-terminal MIM (aa 400–755, KIAA0429) was obtained from the Kazusa DNA Research Institute. The full-length MIM cDNA was amplified through overlap PCR using these N- and C-terminal cDNAs as templates. The cDNAs encoding the full-length human MIM (aa 1–755), MIM-IMD (aa 1–250), and MIM-ΔIMD (aa 251–755) were inserted into pEGFP-C1, pCXN2-FLAG, and pGEX-4T3 or 6P3 vectors.

**Cells and Transfection**—HeLa cells and 293T cells were cultured in Dulbecco's modified Eagle's medium containing 10% fetal bovine serum and 2 mM L-glutamine. HeLa cells and 293T cells were transfected using LipofectAMINE (Invitrogen) according to the manufacturer's protocol.

**Antibodies and Immunofluorescence Analysis**—Rhodamine-conjugated phalloidin and Alexa546-conjugated anti-mouse IgG were purchased from Molecular Probes (Eugene, OR); anti-FLAG M2 antibody was from Sigma-Aldrich. HeLa cells transfected with the plasmids indicated in the figures and cultured for 15–18 h were fixed with 2% formaldehyde in phosphate-buffered saline and permeabilized with 0.1% Triton X-100 in phosphate-buffered saline. The cells transfected with plasmids expressing GFP-tagged proteins were counterstained with rhodamine-phalloidin. The cells transfected with both GFP-tagged protein-expressing vectors and FLAG-tagged small GTPase-expressing

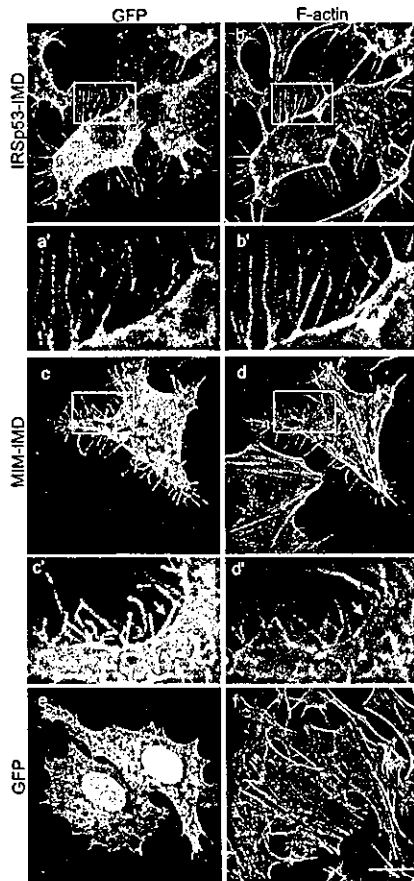


**FIG. 2. The IMDs of IRSp53 and MIM induce filopodia.** HeLa cells were transfected with the GFP-tagged IMD of IRSp53 (panels *a* and *b*), that of MIM (panels *c* and *d*), or GFP alone (panels *e* and *f*). The GFP signal (left column) and F-actin visualized with rhodamine-phalloidin (right column) are shown. Panels *a'*, *b'*, *c'*, and *d'* are enlarged micrographs of rectangular areas of the corresponding figures. The arrows in *c'* and *d'* show accumulation of MIM-IMD in filopodium/microvillus-like protrusions. Scale bar, 20  $\mu$ m. All analyses of cellular phenotypes in this study were based on observations of cells expressing moderate levels of GFP-tagged IRSp53, MIM, or their fragments. High expressers often showed a dendritic phenotype with severe retraction of the cell body and thus were not used for the analyses.

vectors were immunostained with anti-FLAG M2 antibody followed by an Alexa546-conjugated anti-mouse IgG. Fluorescence images were obtained using a confocal microscope (BX50WI, Fluoview, Olympus, Tokyo, Japan) with a water immersion objective lens (LUMPlanFI 60 $\times$ , 0.90 W). To show the entire cell morphology in detail, all of the cell images shown were extended focus images reconstructed from a series of optical sections taken at 0.2–0.3- $\mu$ m intervals.

**F-actin Binding and Bundling Assays**—F-actin was prepared from rabbit skeletal muscle as described (17). Glutathione S-transferase (GST) fusion proteins of various fragments of IRSp53 and MIM (see Fig. 1B) were expressed in BL21-Star (DE3) cells (Invitrogen), purified using glutathione-Sepharose (Amersham Biosciences), and then buffer-exchanged into F buffer (25 mM Hepes, pH 7.5, 100 mM KCl, 0.2 mM CaCl<sub>2</sub>, 2 mM MgCl<sub>2</sub>, 2 mM EGTA, 0.2 mM ATP, 1 mM dithiothreitol) containing 0.1% C<sub>12</sub>E<sub>8</sub> (Nikko Chemicals, Tokyo, Japan). For binding assays, purified GST-fused fragments were clarified by centrifugation at 400,000  $\times$  *g* for 15 min to remove any aggregates, mixed with F-actin in the F buffer, and incubated for 30 min on ice. The final concentration of the GST fusions and F-actin were 1.2 and 5  $\mu$ M (as for G-actin), respectively. The mixture was then centrifuged as above, and equal aliquots of the supernatant and the pellet were analyzed by SDS-PAGE followed by Coomassie Blue staining. For quantitative analysis of F-actin binding and bundling, the IMDs were cleaved out from the GST fusions expressed by pGEX-6P3 vectors using PreScission Protease (Amersham Biosciences) and further purified by cation exchange chromatography (Resource S; Amersham Biosciences). To quantify F-actin binding, increasing amounts of F-actin were incubated with 2  $\mu$ M IRSp53-IMD or MIM-IMD in the F buffer for 3 h at room temperature.

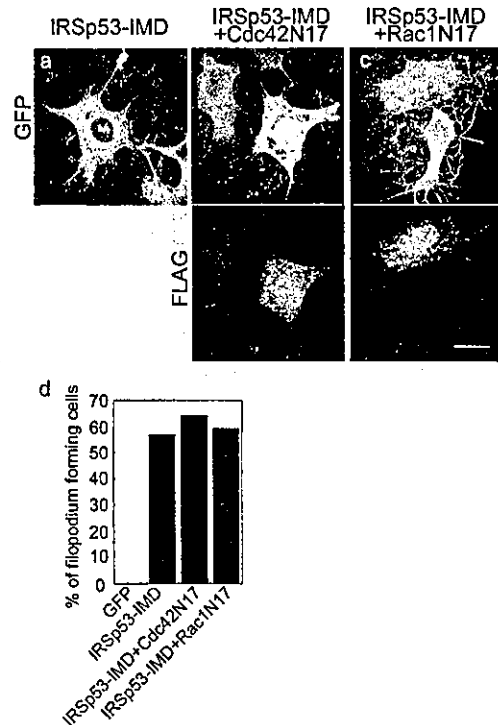


**FIG. 3. The IRSp53-IMD induces filopodia independently of small GTPases.** HeLa cells expressing the GFP-fused IRSp53-IMD (panels *a*–*c*). The cells were co-transfected with FLAG-tagged dominant negative Cdc42N17 (panel *b*) or Rac1N17 (panel *c*). The upper row shows GFP signals, and the lower row shows Cdc42N17 (panel *b*) or Rac1N17 (panel *c*) expression detected by FLAG tag. Scale bar, 20  $\mu$ m. The bar graph in panel *d* shows the frequency of cells developing numerous filopodia in a typical experiment. More than 100 cells were analyzed for each data point. Cells expressing both GFP and FLAG-tagged proteins were analyzed.

The samples were then centrifuged and analyzed as above. The protein bands were quantified by densitometry (Personal Densitometer SI; Amersham Biosciences). For quantitative bundling assay, increasing amounts of the IMDs were incubated with 1  $\mu$ M F-actin in the F buffer for 1 h at room temperature. The supernatant and the pellet were separated by low speed centrifugation (10,000  $\times$  *g* for 30 min) and analyzed as above.

**Observation of Actin Bundles**—For fluorescence microscope observation, a fixed concentration of F-actin (final concentration, 1.2  $\mu$ M) was mixed with variable concentrations of the GST-fused fragments (0.24 to 12  $\mu$ M). After incubation for 30 min on ice in F buffer, F-actin was stained with rhodamine-phalloidin for 15 min on ice. The mixtures were applied to poly-L-lysine-coated glass coverslips and incubated for 20 min at room temperature. The adherent material was washed with F buffer and observed with the confocal laser scanning microscope using an oil immersion objective lens (PlanApo 60 $\times$ , 1.40 oil). For negative staining of actin filaments and bundles, the rhodamine-phalloidin-stained specimens described above were diluted 10 times with F buffer, placed onto a carbon-coated mesh, and stained with 2% uranyl acetate. For observation of thin sectioned specimens, actin bundles formed after incubation for 1 h on ice were packed by centrifugation and fixed in 2.5% glutaraldehyde in 0.1 M cacodylate buffer, pH 7.4, and then sequentially incubated with 0.1% aqueous tannic acid and 0.2% uranyl acetate (18), postfixed in 0.5% aqueous OsO<sub>4</sub>, dehydrated, and embedded in Epon 812. Thin sections stained by lead citrate were examined with a CM 120 electron microscope (Philips Electronics, Eindhoven, The Netherlands) equipped with a multiscan cooled charge-coupled device camera (model 791; Gatan, Pleasanton, CA).

**Cross-linking of Proteins**—One  $\mu$ M of purified IRSp53-IMD, MIM-IMD, and chymotrypsinogen A (Amersham Biosciences) as the control were cross-linked in 0.1 M 2-morpholinoethanesulfonic acid, pH 5.0, at room temperature. The reaction was started by the addition of 4 mM 1-ethyl-3-(3-dimethylaminopropyl) carbodiimide and was stopped by the addition of 50 mM Tris-HCl, pH 8.0, at the time points indicated in Fig. 7A.

**Immunoprecipitation**—293T cells were washed with phosphate-buffered saline and lysed in lysis buffer (100 mM NaCl, 25 mM Hepes, pH



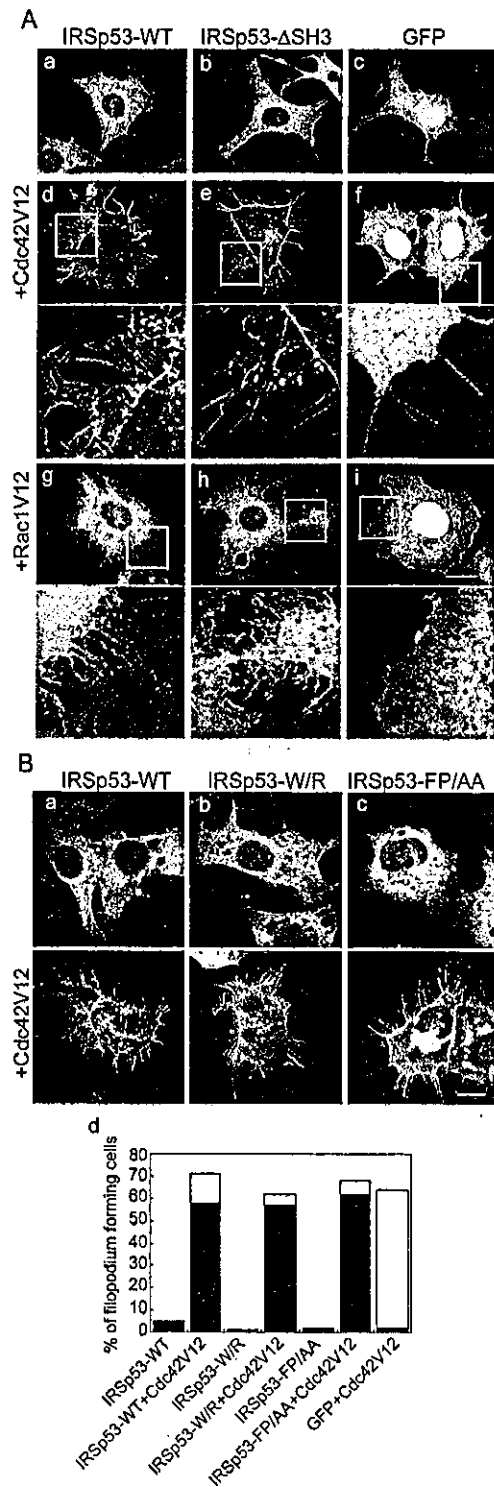


**FIG. 4. The IMD in wild-type IRSp53 is regulated by Cdc42 and Rac1.** A, GFP signals of HeLa cells expressing the GFP-tagged full-length IRSp53 (WT; panels a, d, and g), the GFP-tagged N-terminal half ( $\Delta$ SH3; panels b, e, and h), or GFP alone (GFP; panels c, f, and i). Panels a–c, cells without co-transfection. Panels d–f, cells co-transfected with Cdc42V12. Panels g–i, cells co-transfected with Rac1V12. Enlarged views of the rectangular areas are shown below. Scale bar, 20  $\mu$ m. B, HeLa cells expressing the GFP-tagged full-length IRSp53 (WT; panel a), an SH3 mutant with W417R substitution (W/R; panel b), or another SH3 mutant with F427A/P428A substitutions (FP/AA; panel c). The upper row is without co-transfection, and the lower row shows cells co-transfected with the FLAG-tagged active Cdc42. The expression of Cdc42 was detected by FLAG immunostaining (not shown). Scale bar, 20  $\mu$ m. The stacked bar graph in panel d shows the frequency of cells presenting the IRSp53+Cdc42 phenotype (filled bars) and the Cdc42 phenotype (open bars) in a typical experiment. Cells forming numerous,

7.5, 2 mM MgCl<sub>2</sub>, 2 mM EGTA, 0.5% Triton X-100, containing protease inhibitor mixture; Roche Applied Science). The lysates were precleared by centrifugation at 100,000  $\times$  g for 10 min, followed by immunoprecipitation with a rabbit anti-GFP antibody and protein A-Sepharose beads (Amersham Biosciences). The immunoprecipitates were subjected to SDS-PAGE and immunoblotting with antibodies as indicated in Fig. 7B. The proteins reacting with primary antibodies were visualized by an enhanced chemiluminescence system (Amersham Biosciences) for detecting peroxidase-conjugated secondary antibodies and analyzed with an LAS-1000 system (Fuji Film, Tokyo, Japan).

## RESULTS

*The N-terminal Helical Domain Is Evolutionarily Conserved in IRSp53 Family Proteins and MIM Family Proteins*—IRSp53 and MIM share the N-terminal stretch of 250 amino acids (22% identical, 18% similar), whereas the remaining parts of the molecules show only marginal similarity. To explore whether this similarity is based on real homology, we searched the GenBank™ data base for proteins having similar sequences. First we found three more genes encoding homologous N-terminal sequences in the human genome: insulin receptor tyrosine kinase substrate (IRTKS), the hypothetical gene FLJ22582, and ABBA-1 (Fig. 1A; see the supplemental table for details). IRTKS and FLJ22582 are IRSp53-related proteins containing an SH3 domain in the C-terminal half. However, both of them lack the half-CRIB motif found in IRSp53, and FLJ22582 further lacks the WWB (PPPXY) (Fig. 1B). ABBA-1 (GenBank™ accession number AB115770) is a MIM-related protein that possesses a WH2 domain in the C terminus. Further data base searches have shown that each of these five proteins has a putative ortholog in chicken and zebra fish, indicating that they are well conserved through vertebrate evolution (Supplemental Figs. 1–4). As pointed out previously (9, 13), related proteins are also found in invertebrates (*Caenorhabditis elegans* M04F3.5 protein and *Drosophila melanogaster* CG32082 protein). In an amino acid sequence alignment of the N-terminal region of these proteins (Fig. 1A), clusters of basic amino acids, proline, glycine, and clusters of hydrophobic amino acids are well conserved. There is a signature sequence of ALXEE(R/K)(R/G)RFX<sub>0-1</sub>F(IL) in the C-terminal half of the stretch. As expected from the number of basic amino acid clusters in this domain, the estimated isoelectric points are highly basic, ranging from 8.5 for human MIM to 9.2 for human FLJ22582.

The identity of the N-terminal domain is further supported by predicted secondary structures. The domains are almost purely helical, 82–87% for the IRSp53-related proteins, 96–100% for MIM-related proteins, and intermediate contents of 89 and 87% for M04F3.5 and CG32082, respectively. Helix-breaking amino acid residues at the four breaking sites of the IRSp53-related proteins are also conserved in MIM/ABBA family proteins (asterisks in Fig. 1A). Thus, all of these proteins appear to have a common segmentation pattern of helices, helix I–V (Fig. 1A). Although human IRSp53 lacks helix V, it is predicted to be present in the chicken ortholog.

A phylogenetic tree (Fig. 1C) based on the alignment of the IMDs shows that the vertebrate IRSp53/MIM family is divided into two major groups: the IRSp53 subfamily and the MIM/ABBA subfamily. The putative invertebrate homologs are positioned between them. The tree of the IMDs exactly reflects the hierarchy of domain composition of these proteins. The IRSp53 subfamily members contain an SH3 domain, and the MIM/ABBA subfamily proteins contain a WH2 domain. The

long, wavy, and often branching filopodia (A, panel d for an example) were counted as the IRSp53+Cdc42 phenotype cells. The cells forming long, straight filopodia (A, panel f for an example) were counted as the Cdc42 phenotype cells.

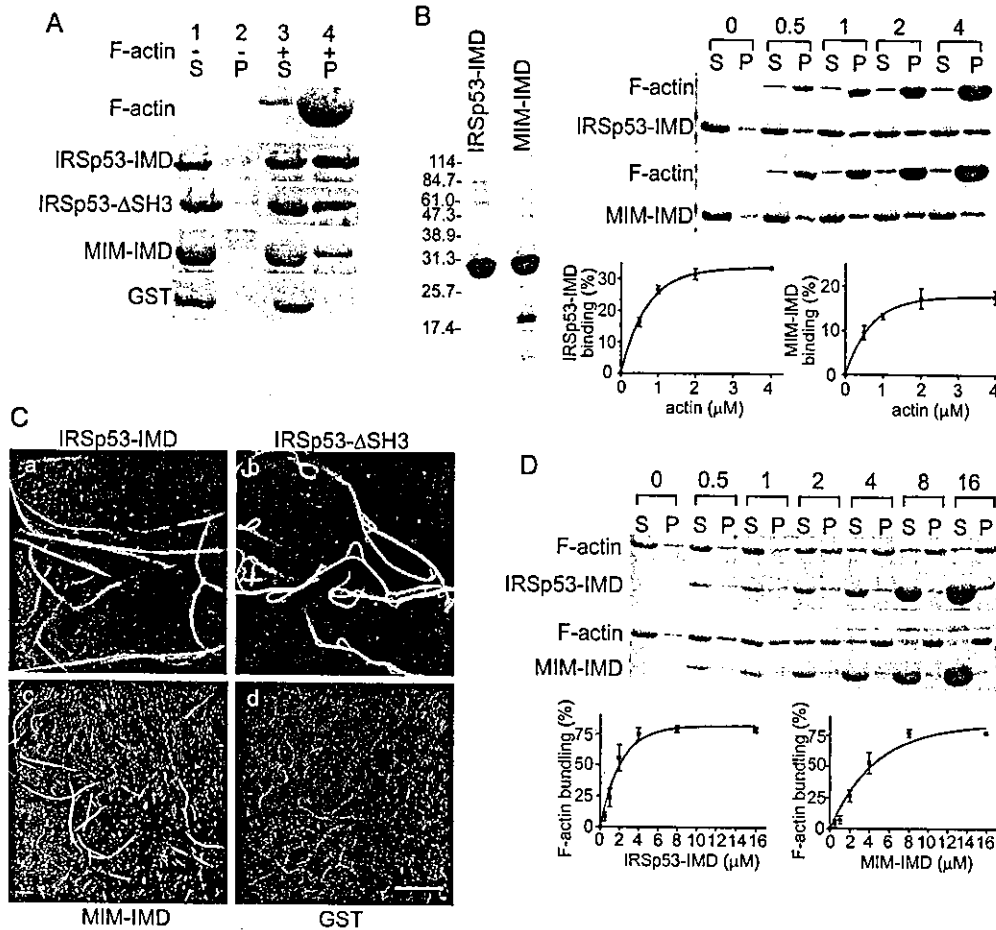


**FIG. 5. F-actin binding/bundling activity of the IRSp53-IMD and MIM-IMD.** *A*, high speed F-actin co-sedimentation assay. 1.2 μM GST-fused IRSp53 fragments (*IRSp53-IMD* and *IRSp53-ΔSH3*), a MIM fragment (*MIM-IMD*), or GST alone (*GST*) were incubated with (+) or without (-) F-actin (5 μM as for G-actin) for 30 min on ice and then ultracentrifuged at 400,000 × *g* for 15 min. Equal aliquots of the supernatant (*S*) and the resuspended pellet (*P*) were analyzed by SDS-PAGE and Coomassie Blue staining. *B*, quantitation of F-actin binding activity of IMDs. Purified tag-free IMDs analyzed by SDS-PAGE are shown in the *left panel*. 2 μM of tag-free IMDs and 0, 0.5, 1, 2, and 4 μM of F-actin were co-sedimented at 400,000 × *g*. The IMD bands stained with Coomassie Blue (*right upper panel* showing a representative data) were quantified by densitometry. The relatively long incubation time used in this experiment caused precipitation of 6–8% of the total IMDs without F-actin. To show the net F-actin binding of the IMDs, the percentage of F-actin-bound IMD was calculated as the percentage recovered in the pellet subtracted by that recovered in the pellet without F-actin. The data shown in the *lower panel* are the means ± S.D. of three independent experiments. *S*, supernatant; *P*, pellet. *C*, visualization of F-actin bundles induced by IMDs. F-actin (1.2 μM) was incubated with 1.2 μM GST-*IRSp53-ΔSH3* (*panel a*), 6 μM GST-*IRSp53-IMD* (*panel b*), 6 μM GST-*MIM-IMD* (*panel c*), or 1.2 μM GST alone (*panel d*) for 30 min on ice. After staining with rhodamine-phalloidin, actin filaments and bundles were observed under a confocal microscope. Scale bar, 10 μm. *D*, quantitation of F-actin bundling activity of IMDs. 0, 0.5, 1, 2, 4, 8, and 16 μM of tag-free IMDs and 1 μM of F-actin were co-sedimented at 10,000 × *g*. 4–10% of total actin was recovered in the pellet in the absence of the IMDs. The percentages of actin in the bundles were quantified as described for Fig. 5*B*. The data shown in the *lower panel* are the means ± S.D. of three independent experiments. *S*, supernatant; *P*, pellet.

vertebrate SH3-containing subfamily is further divided into three groups according to the presence or absence of the WWB and the half-CRIB motif. These data suggest that the IRSp53/MIM family originated from a common ancestor and diverged through evolution. This hypothesis is supported by the fact that IRTKS and FLJ22582 but not M04F3.5 or CG32082 share highly homologous C termini with the MIM/ABBA subfamily members (supplemental Fig. 6). Our analyses suggest the presence of an evolutionarily conserved IRSp53/MIM family and that the IMDs are the key components for the functional roles of proteins belonging to this family.

**The IMDs of IRSp53 and MIM Induce Filopodia in HeLa Cells**—To explore the functional roles of the IMD, we first examined the morphological effects of ectopic expression of the IRSp53-IMD and the MIM-IMD in HeLa cells. The cells expressing the GFP-tagged IMD of IRSp53 formed numerous long filopodia that were F-actin-rich as demonstrated by rhodamine-phalloidin staining (Fig. 2, *panels a, a', b, and b'*). The MIM-IMD also induced filopodia, but they were reduced in length (Fig. 2, *panels c, c', d, and d'*). In addition, MIM-IMD

promoted the formation of microvillus-like protrusions on the apical cell surface. IRSp53-IMD and MIM-IMD localized to and occasionally were concentrated in these protrusions (*arrows* in Fig. 2, *panels c' and d'*). Both IMDs appeared not to be associated with stress fibers. There were no obvious signs of enhanced lamellipodial activity or disruption of stress fibers in these IMD-expressing cells. GFP used as a negative control did not induce any morphological changes (Fig. 2, *panels e and f*). Truncated fragments of IMD, IRSp53-N-IMD (aa 1–161), and IRSp53-C-IMD (aa 105–250) could not stimulate filopodium-formation (data not shown). These data indicate that both IMDs are capable of inducing filopodia in cells. Because IRSp53 and MIM represent the most divergent members of the vertebrate IRSp53/MIM protein family (Fig. 1*C*), the filopodium inducing activity of the IMD is likely to be conserved in all family members.

**IMD Does Not Act Upstream of Rac1 or Cdc42 for Filopodium Formation**—Actin cytoskeletal reorganization is often a hallmark of Rho family GTPases. Previous reports have shown that Rac1 binds to the N terminus of IRSp53 (8) and Cdc42 binds to

the aa 202–305 fragment containing the half-CRIB motif (6). Therefore, we examined whether Cdc42 or Rac1 activation was involved in IMD-induced filopodium formation. The formation of numerous filopodia induced by IRSp53-IMD was not perturbed by the co-expression of dominant negative Cdc42 or Rac1 (Fig. 3). There was no quantitative difference in the ratio of filopodium forming cells among HeLa cells transfected with IRSp53-IMD alone, those transfected with IRSp53-IMD and Cdc42N17, and those transfected with IRSp53 and Rac1N17 (Fig. 3, *panel d*), suggesting that the IMD itself is not regulated by these small GTPases. This result also excludes the possibility that the domain functions upstream of these small GTPases.

**The Filopodium-inducing IMD Activity of Wild-type IRSp53 Is Regulated by Cdc42 and Rac1**—The common mechanism of effector activation by Rho family GTPases appears to be dependent on the disruption of intramolecular autoinhibitory interactions. Cdc42-induced conformational changes have also been demonstrated for the molecule containing a half or semi-CRIB motif, Par6 (19). First we found that GFP-tagged IRSp53-WT or GFP-tagged IRSp53- $\Delta$ SH3, when expressed in moderate levels, could not induce filopodia (Fig. 4A, *panels a–c*). As reported earlier (7, 10), cells expressing very high amounts of IRSp53 often formed dendritic extensions accompanied with severe retraction of the cell body. As noted in the legend to Fig. 2, these cells were omitted from our analyses. Next, we examined whether the IMD function was regulated by Cdc42 and Rac1 in IRSp53-WT and in IRSp53- $\Delta$ SH3 containing the half-CRIB motif. Co-expression of the active Cdc42 with these IRSp53 constructs led to massive formation of wavy filopodia (IRSp53+Cdc42 phenotype as shown in Fig. 4A, *panels d and e*) that was clearly distinguishable from straight filopodia induced in cells co-expressing GFP and active Cdc42 (Cdc42 phenotype as shown in Fig. 4A, *panel f*). A similar level of filopodium induction mixed with Rac1-dependent enhanced lamellipodia activity (Fig. 4A, *panel i*) was induced by the co-expression of active Rac1 (Fig. 4A, *panels g and h*). These results suggest that the SH3 domain is not necessary for IMD-dependent filopodium formation. Our results also suggest that the filopodium-inducing IMD activity in wild-type IRSp53 is regulated by Cdc42 and Rac1. The central region of IRSp53 containing the half-CRIB motif appears to be essential for this regulation, as previously suggested for the regulation of the SH3 domain (7, 9).

To further confirm that the IMD-induced filopodium formation is independent of SH3-binding molecules, we used two nonfunctional SH3 mutants, IRSp53-W/R and IRSp53-FP/AA (7). Both mutants could induce filopodia when expressed with active Cdc42 (Fig. 4B). Although active Cdc42 alone induced filopodium formation in the majority of cells (Fig. 4B, *panel d*, the blank segment in the stacked bar graph reflecting the Cdc42 phenotype), exaggerated filopodium formation, an indication of IMD activity, occurred only when Cdc42 was co-expressed with IRSp53-WT and IRSp53-SH3 mutants (Fig. 4B, *panel d*, the filled segment in the stacked bar graph reflecting the IRSp53+Cdc42 phenotype). Thus, IRSp53 can promote filopodium formation independently of SH3-mediated intermolecular interactions.

**In Vitro F-actin Bundling Activity of IMD**—The filopodium promoting activity of the IMDs of IRSp53 and MIM in cultured cells led us to examine whether these IMDs have F-actin binding and bundling activity. We examined F-actin binding/bundling activity of the GST-fused IMD and other fragments and also tag-free purified IMDs *in vitro*. As shown in Fig. 5A, GST-fused IRSp53-IMD, IRSp53- $\Delta$ SH3, and MIM-IMD but not GST were co-sedimented with F-actin in a high speed assay

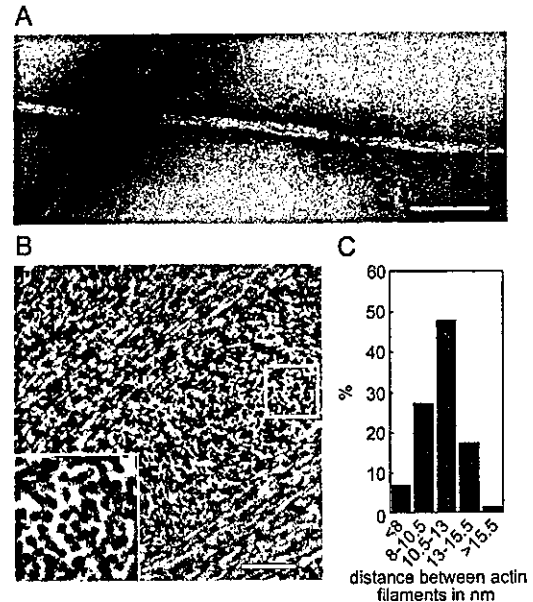


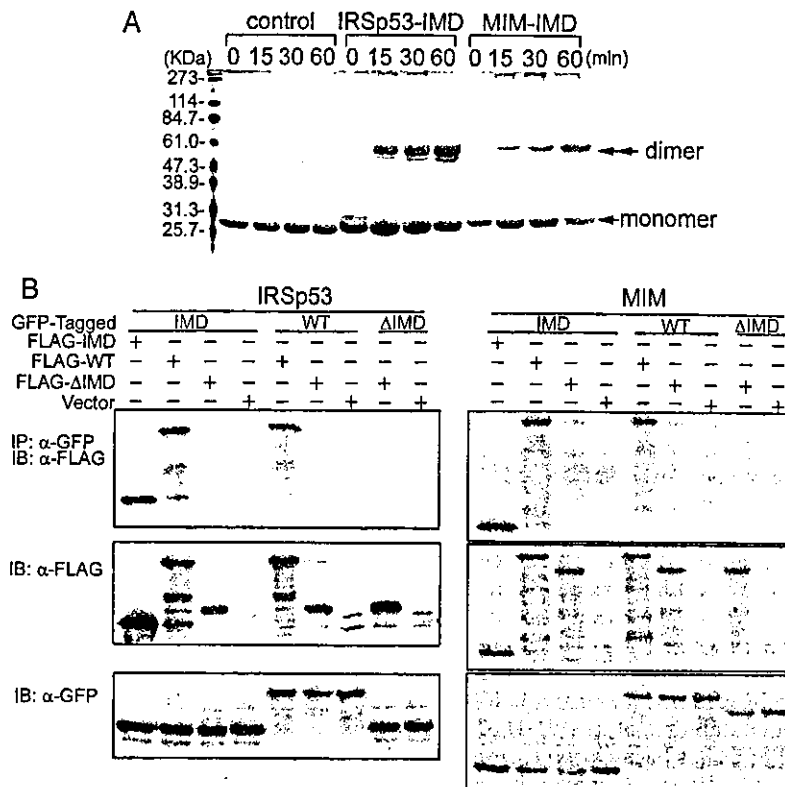
FIG. 6. Electron micrographs of actin bundles induced by IRSp53. A, negatively stained F-actin bundles induced by GST-fused IRSp53-IMD for 30 min on ice. Scale bar, 1  $\mu$ m. B, macroscopically visible tangled threads of actin bundles induced by GST-fused IRSp53- $\Delta$ SH3 for 1 h on ice were packed by ultracentrifugation and processed for transmission electron microscopy. Transverse and longitudinal sections of actin bundles  $\sim$ 0.2  $\mu$ m thick are shown. In a transversely sectioned area (*inset*, enlarged view of the rectangular area), many actin filaments are aligned with a regular center-to-center distance of  $11.2 \pm 2.0$  nm (mean  $\pm$  S.D.,  $n = 854$ ) as shown in C. Scale bar, 0.1  $\mu$ m.

(total binding). To exclude the possible contribution of GST-tag or contaminating bacterial proteins to F-actin binding and bundling, the activities of purified tag-free IMDs (Fig. 5B, *left panel*) were examined. In the high speed assays, the IMDs of IRSp53 and MIM bound to F-actin in a concentration-dependent and saturable manner (Fig. 5B, *right panel*). The apparent half-maximum concentrations of F-actin for IMD binding were almost the same (0.5  $\mu$ M), irrespective of the variation between the maximum extents of these IMDs, suggesting that both IMDs have roughly the same affinity to F-actin. Low levels of the maximum extent of bound IMDs, about 30% for IRSp53-IMD and 20% for MIM-IMD, can be explained by improper protein folding of the bacterially made IMDs or their denaturation during the purification process.

The GST fusions capable of F-actin binding induced thick F-actin bundles (Fig. 5C). Although GFP-tagged IRSp53- $\Delta$ SH3 required activation by Rac1 or Cdc42 for filopodium formation, GST-fused IRSp53- $\Delta$ SH3 alone could induce F-actin bundling. It is possible that the bacterially made protein may not be folded properly to form the self-inhibitory conformation. IRSp53- $\Delta$ SH3 showed stronger bundling than IRSp53-IMD or MIM-IMD; however, different levels of bundling activity among these proteins may simply reflect differences in stability of these fusion proteins. To quantify the bundling activity, the tag-free IMDs were examined in low speed sedimentation assay (Fig. 5D). The bundling activity was concentration-dependent, and most of F-actin could be incorporated into bundles in high concentrations of the IMDs.

The IMD-induced F-actin bundles could be seen under a phase contrast microscope, and their thickness was measured at 0.1–0.2  $\mu$ m by electron microscope observation of negatively stained materials (Fig. 6A). Observation of thin sections of the bundles revealed tight packing of parallel actin filaments in the bundles (Fig. 6B). The bundle as a whole was not a paracrystal in which actin filaments were packed into a hexagonal array with a constant spacing of 11.5 nm, as previously described

**FIG. 7. Self-association of IMDs.** *A*, analysis of cross-linked IMDs by SDS-PAGE. 1  $\mu$ M of tag-free IMDs of IRSp53 and MIM were cross-linked with 4 mM 1-ethyl-3-(3-dimethylaminopropyl) carbodiimide for 0, 15, 30, and 60 min. Chymotrypsinogen A was used as a nondimer control. Equal amounts of protein were analyzed by SDS-PAGE followed by Coomassie Blue staining. An arrow and double arrows point to the monomer and the dimer, respectively. *B*, co-immunoprecipitation assay for self-association of IMDs. GFP-tagged IMD, full-length protein (WT), or  $\Delta$ IMD was co-expressed with FLAG-tagged IMD, WT,  $\Delta$ IMD, or FLAG-vector alone (Vector) in 293T cells. GFP-tagged proteins were immunoprecipitated (IP) using anti-GFP antibody and analyzed by immunoblotting (IB) with anti-FLAG M2 antibody (*top panel*). Expression levels of FLAG-tagged proteins (*middle panel*) and GFP-tagged proteins (*bottom panel*) are shown by immunoblot analyses of total lysates.



(20). However, actin filaments in the bundles tended to be arranged in a line and partly packed into a hexagonal pattern (Fig. 6*B*, inset). The center-to-center distance between neighboring actin filaments aligned in a line was nearly constant and was measured at 11.2 nm in transverse sections (Fig. 6*C*). These observations indicate that IRSp53 acts as a typical parallel actin bundle-forming molecule such as fimbrin and fascin and suggest that the IRSp53/MIM family is a novel actin bundling protein family.

**Self-association of IMD**—Actin bundling activity requires at least two independent F-actin-binding sites or a combination of one binding site plus a self-association site in an actin bundling domain. The ability of IMDs to form dimers or oligomers was examined by chemical cross-linking using zero-length cross-linker 1-ethyl-3-(3-dimethylaminopropyl) carbodiimide. The apparent molecular mass of the tag-free IMDs in SDS-PAGE was progressively shifted from 30 kDa, which matched to the calculated molecular masses of the IRSp53-IMD (28,972 Da) and MIM-IMD (28,640 Da) including a short linker sequence, to the dimer one of 60 kDa (Fig. 7*A*). Both of the tag-free IMDs were effectively cross-linked into dimers but not into trimers or tetramers. This result suggests that the purified IMDs are present as dimers. Next we examined IMD self-association in cultured cells. The IMDs of IRSp53 or MIM could associate with each other and with the full-length molecule but not with the C-terminal half lacking the IMD ( $\Delta$ IMD) in co-transfected 293T cells (Fig. 7*B*). Consistent with the IMD-dependent self-association,  $\Delta$ IMD was not co-immunoprecipitated in any combinations, whereas the full-length IRSp53 and MIM associated with themselves. These results indicate that the IMD is a self-associating domain and suggest that IRSp53 and MIM can be present as dimeric forms in mammalian cells.

#### DISCUSSION

In this study we show that the N-terminal helical domain, the IMD, identified in IRSp53 and MIM, induces filopodium formation *in vivo* and F-actin bundling *in vitro* and suggests that these domains are conserved in an evolutionarily related

protein family, the IRSp53/MIM family. We propose that the IRSp53/MIM family is a novel F-actin bundling protein family that includes invertebrate relatives. Although the family members are largely diverged, each vertebrate member (IRSp53, IRTKS, FLJ22582, MIM, and ABBA) is highly conserved throughout the entire molecule in species ranging from fish to human. They are likely to have a common fundamental function, actin bundle formation, with different mechanisms of regulation.

Parallel actin bundles form the core structure of cellular protrusions such as filopodia, microvilli, and microspikes. These structures are tightly packed, noncontractile bundles cross-linked by a class of F-actin bundling proteins, such as fascin and fimbrin, that determine an  $\sim$ 12-nm spacing between actin filaments (20, 21), and the involvement of such proteins is essential for structure formation (18, 22–24, 26). The other class of bundling proteins, represented by  $\alpha$ -actinin, are found in contractile bundles such as stress fibers. There, they cross-link actin filaments with a wide spacing of about 36 nm (27, 28), which allows myosin II to interact with the actin filaments (29). We have shown that the N terminus of IRSp53 induces *in vitro* formation of tightly packed F-actin bundles of 11-nm spacing. The localization of the N-terminal helical domain of IRSp53 and MIM in filopodia with F-actin but not in stress fibers is consistent with the idea that the protein functions in cells as a parallel F-actin bundling protein.

Our present study indicates that SH3-mediated interactions are not always necessary for IRSp53-induced filopodium formation, and this is consistent with a recent report showing that Mena and vasodilator-stimulated phosphoprotein (VASP) are not essential for this process in B16 melanoma cells (10). However, our results neither rule out the Rac1-IRSp53-WAVE2 or Cdc42-IRSp53-Mena pathway nor exclude any contribution of the C-terminal half to IRSp53 induced F-actin rearrangements. The SH3-mediated interactions could contribute to IRSp53 functions by two possible mechanisms. In the first, as in the classical view of IRSp53 function, SH3 ligands play a crucial

role in actin cytoskeleton dynamics, which may additively or synergistically work with the N-terminal IMD. Among these ligands, Ena/VASP family proteins have been reported to have actin bundling activity associated with the Ena/VASP homology 2 domain (30). Recently IRSp53 has been shown to bind to neural isoforms of espin (31), a novel parallel actin bundling protein originally identified as a component of the Sertoli cell spermatid ectoplasmic specialization (32). The resultant multi-domain actin bundling protein complexes may bundle F-actin with increased efficiency or contribute to changes in F-actin dynamics. Second, the SH3-mediated interaction could determine the localization of IRSp53. Although we and others (10) have shown that IRSp53 is able to self-localize in filopodia using its N terminus, levels of accumulation appear not to be high. Considering that actin bundling proteins require a relatively high molar ratio to actin to function, this level of specificity may not be sufficient to support dynamic behavior of the cell periphery in nontransfected cells. Both WAVE2 and Mena are shown to localize at the filopodial tip (25, 33, 34), again suggesting the functional redundancy of these protein complexes with increased specificity of localization.

Here we show that the activity of the IMD is tightly regulated by Rac1 and Cdc42, in a manner similar to that of the SH3 domain (4, 7). Our results suggest that the central region of IRSp53, including the half-CRIB motif, is essential for the autoinhibition of the IMD. The N terminus (aa 1–178) of IRSp53 has been shown to interact with the region around the half-CRIB motif and inhibit binding of the SH3 domain to Mena (7). The autoinhibitory mechanisms of the IMD and the SH3 domain may work together within the same molecule. Conversely, F-actin association of the IMD and the SH3 ligand binding are likely to activate or stabilize each other.

We propose that IRSp53 is a direct effector of Cdc42 and Rac1, acting in concert with various partner proteins recruited by the SH3 domain. Further analyses are required to evaluate the activities of various IRSp53-partner protein complexes and their specific roles in the regulation of cortical actin dynamics. Although MIM has been shown to interact with protein tyrosine phosphatase delta (13), its regulation remains unknown. Our present study reveals that the IMDs are highly conserved both structurally and functionally. So far we have not found any apparent sequence homology of this domain with known F-actin interacting proteins. Future work including crystallographic studies will be needed to ascertain precise molecular mechanisms for F-actin bundling by the IMDs as well as to clarify their regulation, especially by small GTPases in IRSp53.

**Acknowledgments**—We thank Hiroaki Miki (Institute of Medical Science, Tokyo University, Tokyo) for pEF-BOS-Myc-IRSp53; Masahiko Hibi (Riken Center for Developmental Biology) for Zebrafish cDNA;

Michiyuki Matsuda (Research Institute for Microbial Diseases, Osaka University, Suita) for helpful discussion; Manami Sone and Eiko Moriishi for technical assistance; and Hitomi Shimamoto for preparing the manuscript.

## REFERENCES

- Abbott, M. A., Wells, D. G., and Fallon, J. R. (1999) *J. Neurosci.* **19**, 7300–7308
- Oda, K., Shiratsuchi, T., Nishimori, H., Inazawa, J., Yoshikawa, H., Taketani, Y., Nakamura, Y., and Tokino, T. (1999) *Cytogenet. Cell Genet.* **84**, 75–82
- Yeh, T. C., Ogawa, W., Danielsen, A. G., and Roth, R. A. (1996) *J. Biol. Chem.* **271**, 2921–2928
- Miki, H., Yamaguchi, H., Suetsugu, S., and Takenawa, T. (2000) *Nature* **408**, 732–735
- Takenawa, T., and Miki, H. (2001) *J. Cell Sci.* **114**, 1801–1809
- Govind, S., Kozma, R., Monfries, C., Lim, L., and Ahmed, S. (2001) *J. Cell Biol.* **152**, 579–594
- Krugmann, S., Jordens, I., Gevaert, K., Driessens, M., Vandekerckhove, J., and Hall, A. (2001) *Curr. Biol.* **11**, 1645–1655
- Miki, H., and Takenawa, T. (2002) *Biochem. Biophys. Res. Commun.* **293**, 93–99
- Alvarez, C. E., Sutcliffe, J. G., and Thomas, E. A. (2002) *J. Biol. Chem.* **277**, 24728–24734
- Nakagawa, H., Miki, H., Nozumi, M., Takenawa, T., Miyamoto, S., Wehland, J., and Small, J. V. (2003) *J. Cell Sci.* **116**, 2577–2583
- Lee, Y. G., Macoska, J. A., Korenchuk, S., and Pienta, K. J. (2002) *Neoplasia* **4**, 291–294
- Mattila, P. K., Salminen, M., Yamashiro, T., and Lappalainen, P. (2003) *J. Biol. Chem.* **278**, 8452–8459
- Woodings, J. A., Sharp, S. J., and Machesky, L. M. (2003) *Biochem. J.* **371**, 463–471
- Kelley, L. A., MacCallum, R. M., and Sternberg, M. J. (2000) *J. Mol. Biol.* **299**, 499–520
- Niwa, H., Yamamura, K., and Miyazaki, J. (1991) *Gene (Amst.)* **108**, 193–199
- Nagashima, K., Endo, A., Ogita, H., Kawana, A., Yamagishi, A., Kitabatake, A., Matsuda, M., and Mochizuki, N. (2002) *Mol. Biol. Cell* **13**, 4231–4242
- Spudich, J. A., and Watt, S. (1971) *J. Biol. Chem.* **246**, 4866–4871
- Svitkina, T. M., Bulanova, E. A., Chaga, O. Y., Vignjevic, D. M., Kojima, S., Vasiliev, J. M., and Borisy, G. G. (2003) *J. Cell Biol.* **160**, 409–421
- Garrard, S. M., Capaldo, C. T., Gao, L., Rosen, M. K., Macara, I. G., and Tomchick, D. R. (2003) *EMBO J.* **22**, 1125–1133
- DeRosier, D. J., and Tilney, L. G. (1982) *Cold Spring Harb. Symp. Quant. Biol.* **46**, 525–540
- Volkman, N., DeRosier, D., Matsudaira, P., and Hanein, D. (2001) *J. Cell Biol.* **153**, 947–956
- Bartles, J. R. (2000) *Curr. Opin. Cell Biol.* **12**, 72–78
- DeRosier, D. J., and Tilney, L. G. (2000) *J. Cell Biol.* **148**, 1–6
- Small, J. V., Stradal, T., Vignal, E., and Rottner, K. (2002) *Trends Cell Biol.* **12**, 112–120
- Nozumi, M., Nakagawa, H., Miki, H., Takenawa, T., and Miyamoto, S. (2003) *J. Cell Sci.* **116**, 239–246
- Vignjevic, D., Yarar, D., Welch, M. D., Peloquin, J., Svitkina, T., and Borisy, G. G. (2003) *J. Cell Biol.* **160**, 951–962
- Meyer, R. K., and Aebi, U. (1990) *J. Cell Biol.* **110**, 2013–2024
- Taylor, K. A., Taylor, D. W., and Schachat, F. (2000) *J. Cell Biol.* **149**, 635–646
- Katoh, K., Kano, Y., Masuda, M., Onishi, H., and Fujiwara, K. (1998) *Mol. Biol. Cell* **9**, 1919–1938
- Bachmann, C., Fischer, L., Walter, U., and Reinhard, M. (1999) *J. Biol. Chem.* **274**, 23549–23557
- Sekerkova, G., Loomis, P. A., Changyaleket, B., Zheng, L., Eytan, R., Chen, B., Mugnaini, E., and Bartles, J. R. (2003) *J. Neurosci.* **23**, 1310–1319
- Bartles, J. R., Wierda, A., and Zheng, L. (1996) *J. Cell Sci.* **109**, 1229–1239
- Bear, J. E., Svitkina, T. M., Krause, M., Schafer, D. A., Loureiro, J. J., Strasser, G. A., Maly, I. V., Chaga, O. Y., Cooper, J. A., Borisy, G. G., and Gertler, F. B. (2002) *Cell* **109**, 509–521
- Krause, M., Bear, J. E., Loureiro, J. J., and Gertler, F. B. (2002) *J. Cell Sci.* **115**, 4721–4726

# A novel LIM protein Cal promotes cardiac differentiation by association with CSX/NKX2-5

Hiroshi Akazawa,<sup>1</sup> Sumiyo Kudoh,<sup>2</sup> Naoki Mochizuki,<sup>3</sup> Noboru Takekoshi,<sup>2</sup> Hiroyuki Takano,<sup>1</sup> Toshio Nagai,<sup>1</sup> and Issei Komuro<sup>1</sup>

<sup>1</sup>Department of Cardiovascular Science and Medicine, Chiba University Graduate School of Medicine, Chiba 260-8670, Japan

<sup>2</sup>Department of Cardiology, Kanazawa Medical University, Ishikawa 920-0265, Japan

<sup>3</sup>Department of Structural Analysis, National Cardiovascular Center Research Institute, Osaka 565-8565, Japan

The cardiac homeobox transcription factor CSX/NKX2-5 plays an important role in vertebrate heart development. Using a yeast two-hybrid screening, we identified a novel LIM domain-containing protein, named CSX-associated LIM protein (Cal), that interacts with CSX/NKX2-5. CSX/NKX2-5 and Cal associate with each other both *in vivo* and *in vitro*, and the LIM domains of Cal and the homeodomain of CSX/NKX2-5 were necessary for mutual binding. Cal itself possessed the transcription-promoting activity, and cotransfection of Cal enhanced

CSX/NKX2-5-induced activation of *atrial natriuretic peptide* gene promoter. Cal contained a functional nuclear export signal and shuttled from the cytoplasm into the nucleus in response to calcium. Accumulation of Cal in the nucleus of P19CL6 cells promoted myocardial cell differentiation accompanied by increased expression levels of the target genes of CSX/NKX2-5. These results suggest that a novel LIM protein Cal induces cardiomyocyte differentiation through its dynamic intracellular shuttling and association with CSX/NKX2-5.

## Introduction

*CSX/NKX2-5* is a member of NK homeobox gene family that is conserved in evolution and acts as a DNA-binding transcription activator (Komuro and Izumo, 1993; Lints et al., 1993; Akazawa and Komuro, 2003). During embryogenesis, *CSX/NKX2-5* is expressed predominantly in the heart progenitor cells from the very early stage. Targeted disruption of murine *CSX/NKX2-5* resulted in embryonic lethality due to the arrested looping morphogenesis of the heart tube (Lyons et al., 1995). In addition, mutations of *CSX/NKX2-5* cause human hereditary cardiac malformations associated with atrioventricular conduction disturbance (Schott et al., 1998). These results indicate that *CSX/NKX2-5* plays a pivotal role in normal heart development in mammals.

To understand the mechanisms of how *CSX/NKX2-5* controls cardiac development, it is necessary to elucidate the molecular framework of fine-tuned transcriptional regulation of its distinct target genes. Recently, protein-protein interactions have been recognized to be important in many biological processes. Protein complexes consisting of transcription

factors and cofactors are responsible for transcriptional regulation, and its composition is thought to be the key determinant of specificity and intensity of the reaction. Transcriptional activity of *CSX/NKX2-5* is modulated through physical interaction with other transcription factors such as GATA-4 (Durocher et al., 1997; Lee et al., 1998; Shiojima et al., 1999), SRF (Chen and Schwartz, 1996), and Tbx-5 (Bruneau et al., 2001; Hiroi et al., 2001). Here, we isolated a novel *CSX/NKX2-5*-associated protein by a yeast two-hybrid screening using *CSX/NKX2-5* as a bait. The protein was a novel LIM domain-containing protein, which we named CSX-associated LIM protein (Cal). The LIM domain is a double-zinc finger motif and functions as a module for protein-protein interactions (Dawid et al., 1998; Bach, 2000). Nuclear LIM proteins such as LIM homeodomain proteins and LIM only proteins are directly involved in transcriptional regulation during cell differentiation (Dawid et al., 1998; Bach, 2000). Cytoplasmic LIM proteins are involved in divergent biological processes such as regulation of cytoarchitecture, protein trafficking, and specification of cell polarity (Dawid et al., 1998; Bach,

Address correspondence to Issei Komuro, Dept. of Cardiovascular Science and Medicine, Chiba University Graduate School of Medicine, 1-8-1 Inohana, Chuo-ku, Chiba 260-8670, Japan. Tel.: 81-43-226-2097. Fax: 81-43-226-2557. email: komuro-tyk@umin.ac.jp

Key words: cardiogenesis; homeobox transcription factor; LIM domain; nucleocytoplasmic transport; transcriptional regulation

Abbreviations used in this paper: ANP, atrial natriuretic peptide; Ca<sup>2+</sup>, calcium; Cal, CSX-associated LIM protein; CRP, cysteine-rich protein; LMB, leptomycin B; LPP, lipoma preferred partner; NES, nuclear export signal; SERCA2, sarcoplasmic reticulum Ca<sup>2+</sup>-ATPase 2; trip6, thyroid receptor interacting protein 6.

© The Rockefeller University Press, 0021-9525/2004/02/395/11 \$8.00  
The Journal of Cell Biology, Volume 164, Number 3, February 2, 2004 395–405  
<http://www.jcb.org/cgi/doi/10.1083/jcb.200309159>

395

2000). In regard to muscle development, the roles of cysteine-rich protein (CRP) 3/MLP, which is primarily cytoplasmic, have attracted much attention (Arber et al., 1994). Overexpression of CRP3/MLP in C2C12 myoblasts promoted skeletal myogenesis, whereas inhibition of CRP3/MLP activity by antisense oligonucleotide interrupted terminal differentiation of these cells. Mice homozygous for CRP3/MLP mutation exhibited dilated cardiomyopathy resulted from disrupted cytoarchitecture in cardiomyocytes (Arber et al., 1997). These results indicate the possibility that cytoplasmic LIM proteins regulate cell differentiation as well. Recently, some cytoplasmic LIM proteins have been reported to show nuclear localization. For example, CRP3/MLP associates with nuclear LIM proteins Lmo1 and Apterous (Arber and Caroni, 1996) and basic helix-loop-helix transcription factor MyoD (Kong et al., 1997) as well as cytoskeletal proteins, Zyxin, and  $\alpha$  actinin (Louis et al., 1997). However, the molecular mechanism by which the cytoplasmic LIM proteins are involved in nuclear events remains largely unknown.

Here, we show that Cal functions as a coactivator for CSX/NKX2-5 and fulfills its cooperative function based on its dynamic intracellular shuttling mechanisms. Consistent with the notion that the LIM domains function as an interface of protein-protein interactions, the LIM domains of Cal are required for binding to the homeodomain of CSX/NKX2-5. Cal itself has the transcription-promoting activity and activates the atrial natriuretic peptide (ANP) promoter by forming complex with CSX/NKX2-5. Cal traffics out of the nucleus by nuclear export signal (NES)-dependent mechanisms and traffics into the nucleus in response to an increase of intracellular calcium ( $Ca^{2+}$ ) concentration. Nu-

clear expression of Cal promotes cardiac differentiation of P19CL6 cells in vitro. Characterization of complex formation between CSX/NKX2-5 and Cal will provide a unique framework whereby gene expression during cardiogenesis is fine-tuned by the primarily cytoplasmic LIM proteins that were supposed to be involved in cytoskeletal organization.

## Results

### Molecular cloning and characterization of Cal

To identify proteins that interact with CSX/NKX2-5, we screened a human heart library by the yeast two-hybrid system using the full length of CSX/NKX2-5 as a bait, and isolated a gene out of 25 positive clones, which we named Cal. Using the human Cal cDNA, we isolated the mouse full-length Cal cDNA, which encodes a protein of 375 aa (Fig. 1 A) with three tandemly arrayed LIM domains in the COOH terminus. It contains a region abundant in proline residues in the NH<sub>2</sub> terminus. In addition, there is a leucine-rich motif that matches the consensus sequence for NES. These salient structural features are shared among Zyxin family of LIM domain-containing proteins consisting of Zyxin (Beckerle, 1997), lipoma preferred partner (LPP) (Petit et al., 1996), Ajuba (Goyal et al., 1999), and thyroid receptor interacting protein 6 (trip6; Yi and Beckerle, 1998). Northern blot analysis revealed that there were two transcripts of different sizes, 3.2 and 6.0 kb, and that Cal was highly expressed in a variety of tissues (Fig. 1 B). Most abundant expression was observed in the heart and relatively abundant expression was observed in the lung, intestine, and uterus, whereas little transcript was detected in the brain and liver. RNA in situ hybridization studies revealed that Cal was ex-

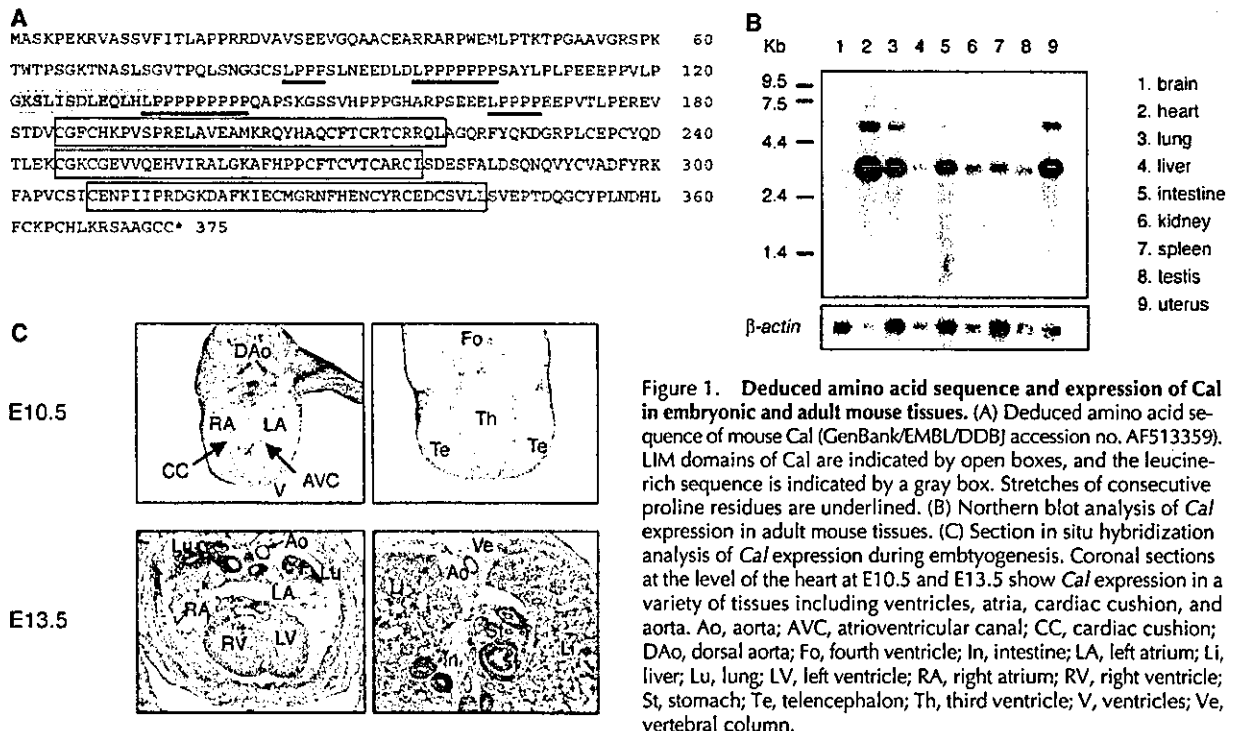


**Figure 1. Deduced amino acid sequence and expression of Cal in embryonic and adult mouse tissues.** (A) Deduced amino acid sequence of mouse Cal (GenBank/EMBL/DBJ accession no. AF513359). LIM domains of Cal are indicated by open boxes, and the leucine-rich sequence is indicated by a gray box. Stretches of consecutive proline residues are underlined. (B) Northern blot analysis of Cal expression in adult mouse tissues. (C) Section in situ hybridization analysis of Cal expression during embryogenesis. Coronal sections at the level of the heart at E10.5 and E13.5 show Cal expression in a variety of tissues including ventricles, atria, cardiac cushion, and aorta. Ao, aorta; AVC, atrioventricular canal; CC, cardiac cushion; DAo, dorsal aorta; Fo, fourth ventricle; In, intestine; LA, left atrium; Li, liver; Lu, lung; LV, left ventricle; RA, right atrium; RV, right ventricle; St, stomach; Te, telencephalon; Th, third ventricle; V, ventricles; Ve, vertebral column.

pressed in a wide variety of cell-lineages including the heart, lung, and intestine during mouse embryogenesis (Fig. 1 C). Lesser transcript was observed in the liver, and no transcript was observed in the vertebral column and encephalon.

### Cal forms a complex with CSX/NKX2-5

To examine whether CSX/NKX2-5 and Cal directly interact with each other *in vivo*, we cotransfected COS7 cells with HA-tagged CSX/NKX2-5 and FLAG-tagged Cal. Cell lysates were subjected to immunoprecipitation using anti-FLAG antibody, and coprecipitating CSX/NKX2-5 was detected by immunoblotting with anti-HA antibody (Fig. 2 A). This result suggests that CSX/NKX2-5 and Cal associate with each other in mammalian cells as well as yeast cells.

Next, to confirm the direct interaction between CSX/NKX2-5 and Cal, and if so, to determine the domain responsible for the association, GST pull-down assays were performed with GST-Cal fusion protein and *in vitro*-translated CSX/NKX2-5. GST-Cal immobilized on glutathione-Sepharose beads retained *in vitro*-translated CSX/NKX2-5, indicating the direct interaction between CSX/NKX2-5 and Cal (Fig. 2 B). A CSX/NKX2-5 mutant lacking the homeodomain did not associate with Cal, but the homeodomain of CSX/NKX2-5 was enough for association (Fig. 2 B). These results suggest that the homeodomain of CSX/NKX2-5 is necessary and sufficient for the interaction with

Cal. We also examined the binding of GST-CSX/NKX2-5 and *in vitro*-translated Cal and its mutants. A Cal mutant lacking all three LIM domains did not associate with CSX/NKX2-5, but Cal mutants containing at least two LIM domains did associate with CSX/NKX2-5 (Fig. 2 C). These results suggest that the LIM domains of Cal are responsible for interaction with CSX/NKX2-5.

### CSX/NKX2-5 and Cal synergistically transactivate the ANP promoter

To examine the effect of Cal on transcriptional activity of CSX/NKX2-5, we performed a series of reporter assays using the luciferase reporter linked to the ANP promoter. When the luciferase construct containing the ANP promoter was cotransfected with CSX/NKX2-5 expression vector, significant fold induction of the promoter activity was observed as reported previously (Shiojima et al., 1999). Although overexpression of Cal had no effect on the ANP promoter, cotransfection of Cal with CSX/NKX2-5 induced much stronger transactivation than CSX/NKX2-5 alone, suggesting that CSX/NKX2-5 and Cal synergistically transactivate the ANP promoter (Fig. 3 A). CSX/NKX2-5 and Cal also synergistically transactivated the luciferase construct containing multimerized CSX/NKX2-5-binding sites (Fig. 3 A).

Next, we examined whether the interaction between CSX/NKX2-5 and Cal was required for the synergistic

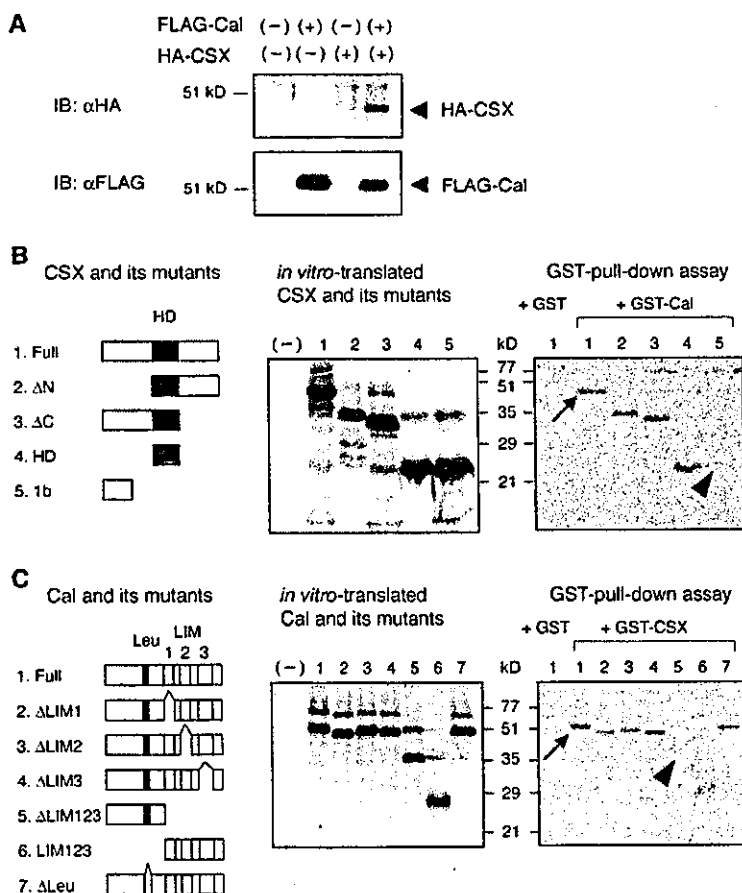


**Figure 2. Complex formation between CSX/NKX2-5 and Cal.** (A) Coimmunoprecipitation of CSX/NKX2-5 and Cal in transfected COS7 cells. Immunoprecipitates with anti-FLAG antibody were separated by SDS-PAGE and immunoblotted with anti-HA antibody (top). The same blot was reprobed with anti-FLAG antibody to confirm the presence of FLAG-tagged Cal (bottom). (B) GST pull-down assay for mapping of a region in CSX/NKX2-5 required for binding to Cal. *In vitro*-translated CSX/NKX2-5 and its mutants labeled with  $^{35}$ S were incubated with GST-Cal immobilized on glutathione-Sepharose beads, and bound proteins were separated by SDS-PAGE and visualized by autoradiography. The arrow indicates the CSX/NKX2-5 protein bound to GST-Cal. A CSX/NKX2-5 mutant lacking the homeodomain did not associate with Cal (arrowhead), whereas a CSX/NKX2-5 mutant containing only the homeodomain did associate. HD, homeodomain. (C) GST pull-down assay for mapping of a region in Cal required for binding to CSX/NKX2-5. *In vitro*-translated Cal and its mutants labeled with  $^{35}$ S were incubated with GST-CSX/NKX2-5. The arrow indicates the Cal protein bound to GST-CSX/NKX2-5. A Cal mutant lacking all the LIM domains did not associate with CSX/NKX2-5 (arrowhead), whereas a Cal mutant containing only the LIM domains did associate.



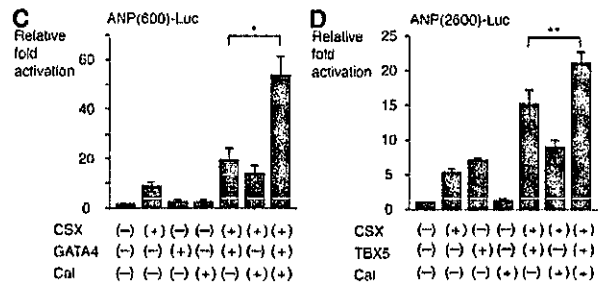
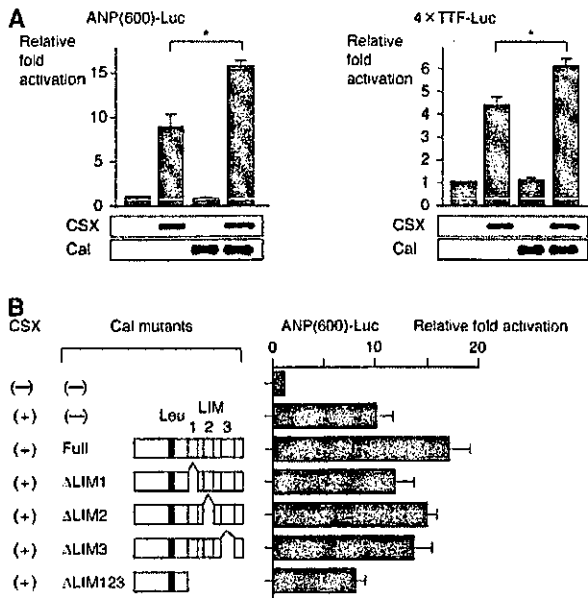


**Figure 3. Cooperative activation of the ANP promoter by CSX/NKX2-5 and Cal.** (A) CSX/NKX2-5 and Cal synergistically transactivate the ANP promoter and CSX/NKX2-5-dependent promoter. The luciferase reporters containing the ANP promoter (ANP[600]-Luc) or multimerized CSX/NKX2-5 binding sites (4xTTF-Luc) were cotransfected in COS7 cells with the expression vectors of CSX/NKX2-5 and/or Cal. An increase in luciferase activities was observed when the CSX/NKX2-5 expression vector was cotransfected with the Cal expression vector. The equivalent expression levels of each construct were confirmed by Western blotting using parallel samples after transfection. The results are expressed as the mean ± SEM. \*, P < 0.01. (B) Synergistic transactivation of the ANP promoter is dependent on the interaction between CSX/NKX2-5 and Cal. A Cal mutant lacking all three LIM domains, the docking module for binding to CSX/NKX2-5, exhibited no significant cooperation on CSX/NKX2-5-induced promoter activation. The results are expressed as the mean ± SEM. (C) Cal augments synergistic transactivation between CSX/NKX2-5 and GATA-4. COS7 cells were cotransfected with the luciferase reporter containing the ANP promoter (ANP[600]-Luc) and the expression vectors of CSX/NKX2-5 and/or GATA-4 and/or Cal. Cotransfection with CSX/NKX2-5 and GATA-4 exhibited synergistic transactivation, that was further enhanced by additional expression of Cal. The results are expressed as the mean ± SEM. \*, P < 0.01. (D) Cal augments synergistic transactivation between CSX/NKX2-5 and Tbx-5. Cotransfection with CSX/NKX2-5 and Tbx-5 exhibited synergistic transactivation of the ANP promoter (ANP[2600]-Luc), that was further augmented by additional expression of Cal. The results are expressed as the mean ± SEM. \*\*, P < 0.05.

transactivation of the ANP promoter. Although Cal mutants lacking one LIM domain, which retain the ability to bind to CSX/NKX2-5, showed synergistic activation with CSX/NKX2-5 on the ANP promoter, the Cal mutant lacking the three LIM domains, which does not bind to CSX/NKX2-5, exhibited no significant cooperation on CSX/NKX2-5-induced promoter activation (Fig. 3 B). These results suggest that the synergistic transactivation was dependent on the mutual binding between CSX/NKX2-5 and Cal.

It has been reported that CSX/NKX2-5 and a zinc-finger transcription factor, GATA-4, display synergistic transcriptional activation of the ANP promoter (Durocher et al., 1997; Lee et al., 1998; Shiojima et al., 1999). As shown in Fig. 3 C, Cal augmented this synergistic promoter activation between CSX/NKX2-5 and GATA4. We and others reported recently that CSX/NKX2-5 and a T-box transcription factor, Tbx-5, showed synergistic transcriptional activation of the ANP promoter (Bruneau et al., 2001; Hiroi et al., 2001). Cal also augmented this synergistic promoter activation between CSX/NKX2-5 and Tbx-5 (Fig. 3 D).

**Cal is a transactivator**

To understand how Cal exhibits synergistic transcriptional activation with CSX/NKX2-5, we examined the transcriptional activity of Cal. The expression vector containing Cal fused to GAL4 DNA-binding domain was cotransfected in COS7 cells with the luciferase reporter containing the multimerized GAL4-binding sites. As shown Fig. 4, full length of Cal fused to the DNA-binding domain of GAL4 transactivated a GAL4-dependent reporter ~13.0-fold com-

pared with DNA-binding domain of GAL4 alone. Cal mutants lacking all three LIM domains, LIM2 or LIM3 domains showed no transcriptional activity, whereas the Cal mutant containing only LIM2 and LIM3 domains showed stronger activity than the full length of Cal. Deletion of LIM1 domain showed even stronger activity, suggesting that Cal itself has the transcription-promoting activity and that its transactivation domain is localized

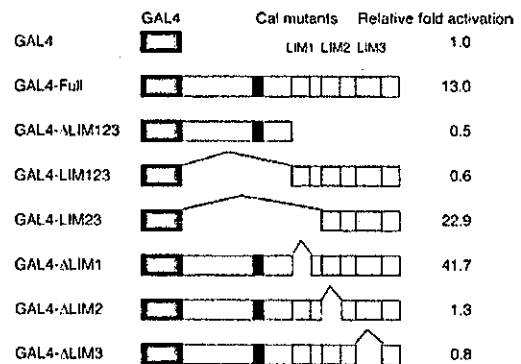


**Figure 4. Transcriptional activity of Cal.** Expression vectors encoding the GAL4 DNA binding domain fused to the indicated regions of Cal were transiently transfected into COS7 cells with the pG5luc-luciferase reporter, which contained five GAL4 binding sites. Cal fused to the DNA binding domain of GAL4 significantly transactivated a GAL4-dependent reporter, indicating that Cal possesses transcriptional activity. Cal mutants lacking LIM2 or LIM3 showed no transcriptional activity, whereas Cal mutants containing LIM2 and LIM3 showed stronger activity.

Downloaded from www.jcb.org on January 26, 2005

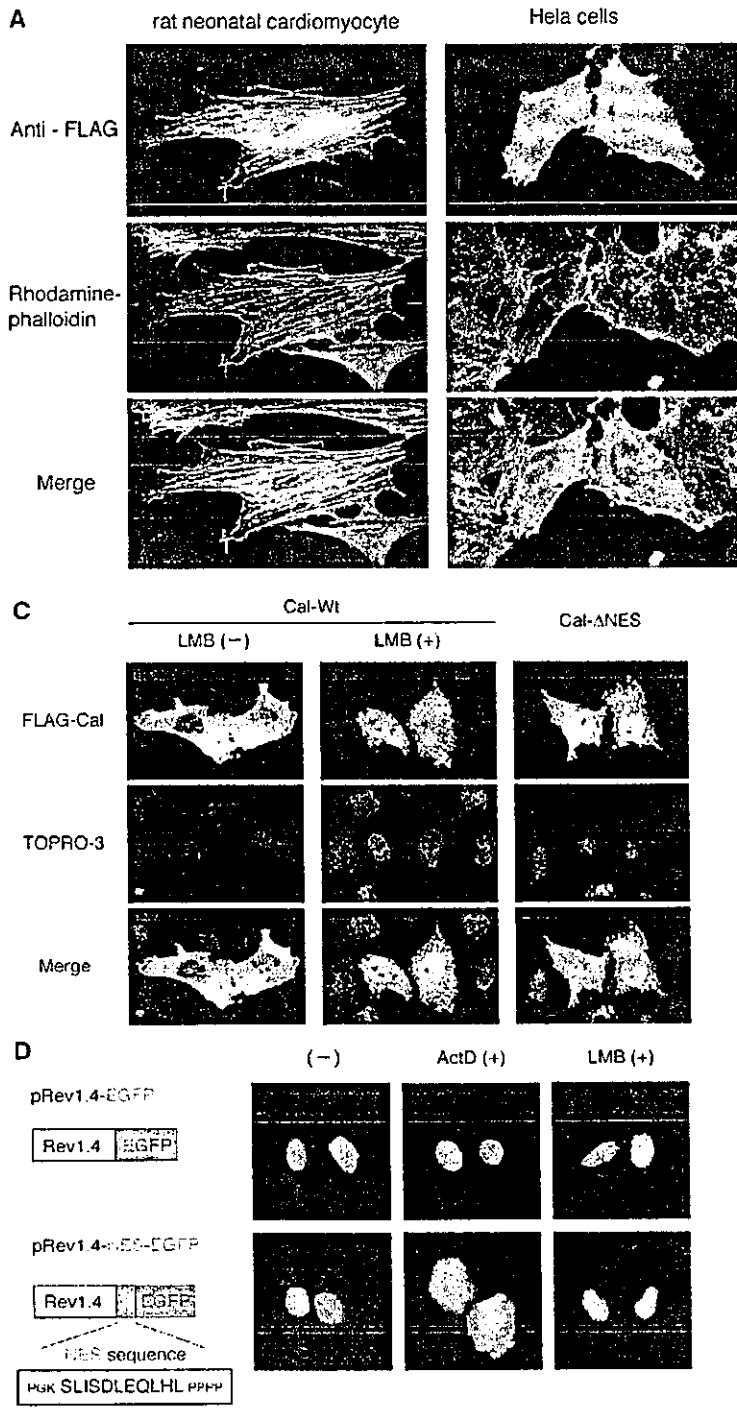


**Figure 5. Subcellular localization of Cal regulated by a leucine-rich NES.** (A) Rat neonatal cardiac myocytes and HeLa cells were transiently transfected with FLAG-tagged Cal expression vector, and cells were stained with anti-FLAG antibody followed by anti-mouse IgG conjugated with FITC (top, green) and rhodamine-phalloidin (middle, red). The bottom panel is a merged image of the top and middle panels and reveals that Cal is localized predominantly in the cytoplasm. (B) NES sequences of Cal and representative proteins are aligned. Leucine residues are boxed in black, and other important hydrophobic residues are boxed in dark gray. (C) HeLa cells, transfected with FLAG-tagged Cal expression vector (Cal-Wt), were treated with 20 ng/ml LMB for 3 h, fixed, and stained with anti-FLAG antibody. LMB treatment induces nuclear accumulation of the Cal protein, indicating the important role of the putative NES in nuclear export of Cal. Consistent with the LMB study, a Cal mutant lacking this sequence (Cal-ΔNES) is localized predominantly in the nucleus. (D) Nuclear export assay based on Rev shuttling system. Rev1.4 is a NES-deficient mutant of HIV-Rev protein, and robust nuclear localization of Rev1.4-EGFP fusion protein is observed even when cells are treated with 5 mg/ml actinomycin D (ActD), which prevents nucleolar association of HIV-Rev. The putative NES of Cal was subcloned into pRev1.4-EGFP vector (pRev1.4-NES-EGFP), and HeLa cells were transiently transfected with pRev1.4-NES-EGFP. The NES of Cal is functional, because Rev1.4-NES-Cal is localized also in the cytoplasm, especially after treatment with ActD.

Downloaded from www.jcb.org on January 26, 2005

within the LIM2 and LIM3 domains, whereas LIM1 may function as a repressor domain.

#### Cal is predominantly localized in the cytoplasm and shuttles between the cytoplasm and the nucleus

We examined the subcellular localization of Cal protein in cultured cells. Cultured cardiac myocytes of neonatal rats were transiently transfected with FLAG-tagged Cal expression vector, and immunofluorescence analysis was per-

formed using anti-FLAG antibody. Cal protein was predominantly localized in the cytoplasm of cardiac myocytes at steady state (Fig. 5 A). Similar pattern of immunofluorescence was obtained in other cell lines such as HeLa (Fig. 5 A), COS7, and NIH3T3 cells (not depicted).

Within the amino acid sequence of Cal, there was a leucine-rich sequence that matched the consensus sequence of NES (Fig. 5 B). During a nuclear export cycle, an exportin molecule CRM1 recognizes the NES and forms a complex

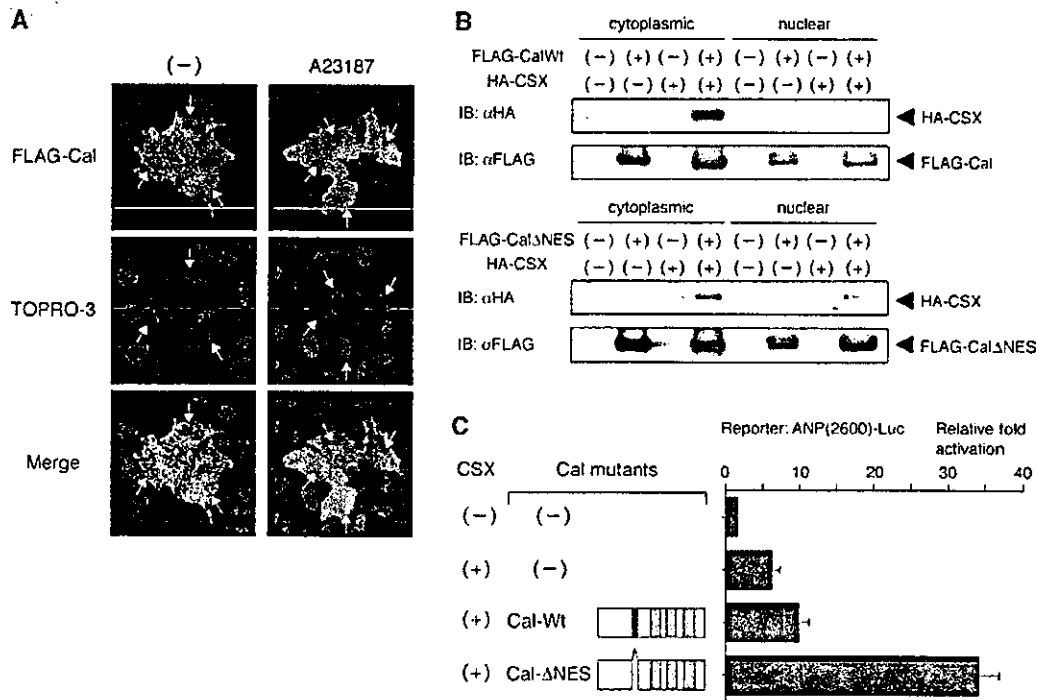


**Figure 6. Nuclear transport of Cal in response to calcium ionophore and implications of nuclear accumulation of Cal in transcriptional cooperativity with CSX/NKX2-5.** (A) HeLa cells, transfected with FLAG-tagged Cal expression vector, were treated with vehicle or calcium ionophore A23187 (2  $\mu$ M) for 15 min, fixed, and stained with anti-FLAG antibody. Nuclear accumulation of Cal is observed in significant portions of transfected cells after treatment with A23187. The arrows indicate the nuclei of the transfected cells. (B) Coimmunoprecipitation of CSX/NKX2-5 and Cal (Cal-Wt) or nuclear form of Cal (Cal- $\Delta$ NES) in preparations of cytoplasmic or nuclear fractions of transfected COS7 cells. Cal- $\Delta$ NES showed significantly stronger interaction with CSX/NKX2-5 in the nucleus than Cal-Wt. (C) The luciferase reporter containing the ANP promoter was cotransfected in COS7 cells with the expression vectors of CSX/NKX2-5 and Cal-Wt or Cal- $\Delta$ NES. Cal- $\Delta$ NES showed much stronger synergistic activation with CSX/NKX2-5 than Cal-Wt. The results are expressed as the mean  $\pm$  SEM.

with RanGTP, and mediates transport to the cytoplasm (Fornerod et al., 1997; Mattaj and Englmeier, 1998; Ohno et al., 1998; Kuersten et al., 2001). NES-dependent nuclear export is inhibited by leptomycin B (LMB) that interferes with the binding of CRM1 to NES (Kudo et al., 1998). Inhibition of CRM1-dependent nuclear export using LMB resulted in rapid nuclear accumulation of Cal protein in HeLa cells (Fig. 5 C). Although immunofluorescence studies indicated that the main compartment where Cal is localized at steady state was the cytoplasm, the accumulation of CAL after treatment with LMB suggested that Cal can shuttle between the cytoplasm and the nucleus.

To confirm that the putative NES contributes to nuclear export of Cal, we deleted the NES sequence (residues 123–132) in the FLAG-tagged Cal expression vector (Cal- $\Delta$ NES) and examined the subcellular localization of Cal- $\Delta$ NES mutant. Cal- $\Delta$ NES was predominantly localized in the nucleus (Fig. 5 C), suggesting that this sequence mediates the CRM1-dependent nuclear export of Cal. To test this sequence of Cal functions as an NES, we introduced this sequence into the export-deficient form of Rev-EGFP, and tested its nuclear export activity in HeLa cells. The putative NES of Cal displayed the export activity, especially in the presence of actinomycin D, which prevents nucleolar association of Rev protein (Fig. 5 D). These results indicate that this 123–132-amino acid sequence of Cal really functions as an NES.

**Cal shuttles into the nucleus in response to  $Ca^{2+}$  signal**  
We explored a specific signal capable of targeting Cal protein to the nucleus. When intracellular  $Ca^{2+}$  levels were increased by  $Ca^{2+}$  ionophore A23187, Cal protein was transported to the nucleus (Fig. 6 A). Nuclear accumulation of Cal was detected at 10 min after addition of A23187. No other cellular signals possessed ability to transport Cal into the nucleus. For example, treatment with cytochalasin D, an actin filament disrupting reagent, tetradecanoylphorbol 13-acetate, PKC activator, forskolin, an adenylate cyclase activator, anisomycin, Jun-NH<sub>2</sub>-terminal kinase agonist, okadaic acid, a serine/threonine phosphatase inhibitor did not induce nuclear translocation of Cal protein.

Next, we examined whether nucleocytoplasmic shuttling of Cal protein had important implications for modifying the transcriptional activity of CSX/NKX2-5. As indicated by coimmunoprecipitation experiments by using cytoplasmic and nuclear fractions of transfected cells, interaction between CSX/NKX2-5 and wild-type of Cal (Cal-Wt) was detectable predominantly in the cytoplasm and slightly in the nucleus (Fig. 6 B). When Cal- $\Delta$ NES, which lacks the NES and is predominantly localized in the nucleus, was cotransfected, the level of coprecipitating CSX/NKX2-5 in the nuclear fraction increased significantly (Fig. 6 B). Furthermore, Cal- $\Delta$ NES showed much stronger synergistic transactivation of the ANP promoter than Cal-Wt, when cotransfected with CSX/

NKX2-5 (Fig. 6 C). These results suggest that nuclear translocation of Cal enhances CSX/NKX2-5-induced promoter activation by promoting mutual interaction in the nucleus.

### Nuclear accumulation of Cal induces cardiac differentiation of P19CL6 cells

To determine whether synergistic transactivation by Cal has a significant effect on cardiomyocyte differentiation, we isolated P19CL6 clones, which stably overexpress wild-type Cal (P19CL6-Cal-Wt) or Cal mutant lacking the NES (P19CL6-Cal- $\Delta$ NES). When cultured in the medium containing 1% DMSO, P19CL6 cells differentiated into cardiomyocytes, which exhibit spontaneous beating and express cardiac-specific genes (Monzen et al., 1999). The expression of cardiac-specific genes was examined in P19CL6 cells, P19CL6-Cal-Wt, and P19CL6-Cal- $\Delta$ NES during differentiation (Fig. 7 A). Northern blot analysis revealed that expression levels of a cardiac transcription factor *GATA-4* and sarcoplasmic reticulum  $Ca^{2+}$ -ATPase 2 (*SERCA2*) as well as *connexin 43* and *calreticulin*, known as downstream targets for CSX/NKX2-5, were increased in P19CL6-Cal- $\Delta$ NES cells. RT-PCR analysis revealed that expression of *ANP* gene was also up-regulated in P19CL6-Cal- $\Delta$ NES cells, which was consistent with the results that Cal augmented *ANP* promoter activation induced by CSX/NKX2-5. Immunocytochemical analysis revealed that in P19CL6-Cal- $\Delta$ NES, a larger number of cells were stained positive with anticardiac troponin T antibody than the parental P19CL6 cells (Fig. 7 B), suggesting that nuclear accumulation of Cal strongly promotes cardiac differentiation.

## Discussion

### Cal is a novel LIM domain-containing protein

We identified a novel protein Cal, which associates with the cardiac homeobox transcription factor CSX/NKX2-5. Cal is a member of Zyxin family, that commonly have a proline-rich region at the NH<sub>2</sub> terminus, a leucine-rich sequence, and three tandem LIM domains located at the COOH terminus. The proline-rich regions of Zyxin serve as interface to bind to SH3 domain of Vav (Hobert et al., 1996) and EVH1 domain of Ena/VASP family proteins (Renfranz and Beckerle, 2002) that are implicated in control of actin organization (Gertler et al., 1996). LPP also contains proline-rich motifs that are required for the interaction with the EVH1 domain (Prehoda et al., 1999). This proline-rich region of LPP directly interacts with VASP in vitro, and LPP is colocalized with VASP in the focal adhesion. The proline-rich regions of Ajuba interact with Grb2 (Goyal et al., 1999). Expression of Ajuba enhances MAPK activity in fibroblasts and promotes meiotic maturation of *Xenopus* oocytes through activation of MAPK in Grb2- and Ras-dependent manner (Goyal et al., 1999). The NH<sub>2</sub>-terminal portion of Cal also contains stretches of proline-rich sequences. Especially, two proline-rich sequences (LPPPPPPP 98-105 and LPPPPPPPPP 133-142) of Cal lead us to speculate that Cal might associate with profilin and be involved in the organization of cytoskeletal actin in the cytoplasm because the sequence of consecutive prolines flanked by leucine has been thought to be a ligand motif for profilin (Ma-

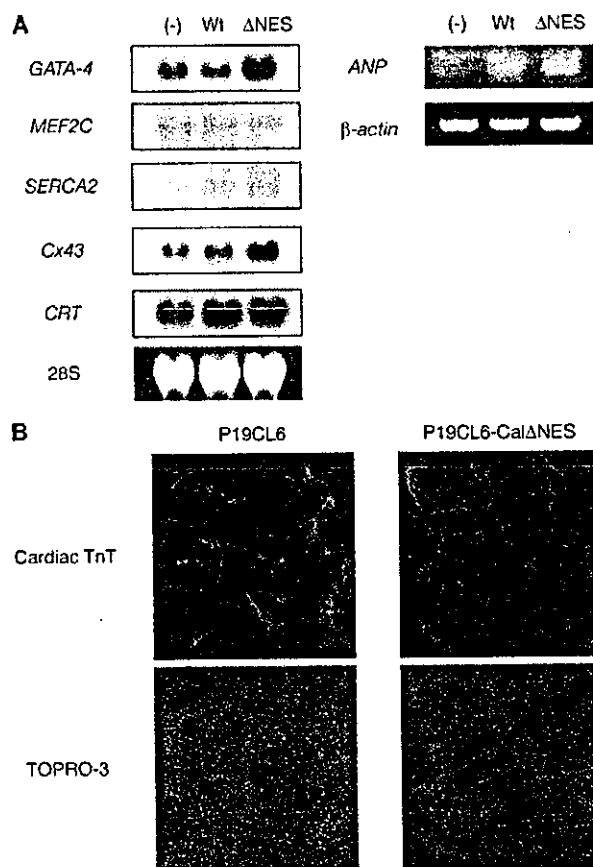


Figure 7. Promotion of cardiac differentiation in P19CL6 cells by nuclear accumulation of Cal. (A) Expression of cardiac genes was examined on differentiation day nine of P19CL6 cells, P19CL6 cells stably expressing Cal-Wt and Cal- $\Delta$ NES. Northern blot analysis was performed with *GATA-4*, *MEF2C*, *SERCA2*, *Connexin43* (*Cx43*), and *calreticulin* (*CRT*) cDNAs and RT-PCR was performed using specific primers for *ANP*. Notably, expression levels of target genes for CSX/NKX2-5 such as *Cx43*, *CRT*, and *ANP* were increased in P19CL6-Cal- $\Delta$ NES. (B) Cardiac differentiation in P19CL6 cells on differentiation day 14 was determined by immunofluorescence with anticardiac troponin T (TnT) antibody. Much larger number of cells were stained positive for cardiac TnT in P19CL6-Cal- $\Delta$ NES.

honey et al., 1997). Identification of proteins binding to the proline-rich region of Cal would provide further insights into its cellular function.

### Cal interacts with CSX/NKX-2.5 both in vitro and in vivo

GST pull-down assays and coimmunoprecipitation experiments indicated the association of Cal with CSX/NKX2-5 both in vitro and in vivo. Analyses using mutants of both proteins revealed that the mutual binding was mediated through the homeodomain of CSX/NKX2-5 and the LIM domains of Cal. Besides binding to DNA, the homeodomain of CSX/NKX2-5 acts as a module for the interaction with its binding partner such as *GATA-4* (Durocher et al., 1997; Lee et al., 1998; Shiojima et al., 1999), *SRF* (Chen and Schwartz, 1996), and *Tbx-5* (Hiroi et al., 2001). The LIM domains of Cal have a cysteine-histidine rich, double zinc-finger motif that functions as a protein-protein in-